



Water Resources Research®

RESEARCH ARTICLE

10.1029/2025WR041300

Key Points:

- We developed a new micro-continuum model to simulate heat transfer, fluid flow, and rock deformation in multiscale porous systems
- The model was validated against analytical solutions and established heat transfer solvers
- This tool supports simulations for energy, environmental, and hydrological applications in complex geological settings

Supporting Information:

Supporting Information may be found in the online version of this article.

Correspondence to:

X. Zheng and I. C. Bourg,
xiaojin.zheng@princeton.edu;
bourg@princeton.edu

Citation:

Zheng, X., & Bourg, I. C. (2025). A multiscale approach to simulate non-isothermal multiphase flow in deformable porous materials. *Water Resources Research*, 61, e2025WR041300. <https://doi.org/10.1029/2025WR041300>

Received 10 JUN 2025

Accepted 6 NOV 2025

Author Contributions:

Conceptualization: Ian C. Bourg
Data curation: Xiaojin Zheng
Formal analysis: Xiaojin Zheng, Ian C. Bourg
Funding acquisition: Ian C. Bourg
Investigation: Xiaojin Zheng
Methodology: Xiaojin Zheng, Ian C. Bourg
Project administration: Ian C. Bourg
Resources: Ian C. Bourg
Software: Xiaojin Zheng
Supervision: Ian C. Bourg
Validation: Xiaojin Zheng
Visualization: Xiaojin Zheng
Writing – original draft: Xiaojin Zheng

© 2025. The Author(s).

This is an open access article under the terms of the [Creative Commons Attribution-NonCommercial-NoDerivs License](#), which permits use and distribution in any medium, provided the original work is properly cited, the use is non-commercial and no modifications or adaptations are made.

A Multiscale Approach to Simulate Non-Isothermal Multiphase Flow in Deformable Porous Materials

Xiaojin Zheng¹  and Ian C. Bourg^{1,2} 

¹Department of Civil and Environmental Engineering, Princeton University, Princeton, NJ, USA, ²High Meadows Environmental Institute, Princeton University, Princeton, NJ, USA

Abstract Coupled thermal, hydraulic, and mechanical processes in porous materials play important roles in several energy and environmental technologies. The Darcy-Brinkman-Biot (DBB) framework has proven effective in modeling multiphase fluid flow in deformable porous solids across both pore and Darcy scales, including in systems where fractures coexist with a porous matrix. In this study, we extend the DBB framework, originally designed for isothermal conditions, to address non-isothermal problems by incorporating an energy conservation equation. The resulting solver, *hybridBiotThermalInterFoam*, enables simulations of coupled multiphase fluid flow, heat transfer, and solid deformation in hybrid-scale systems containing both solid-free regions and ductile porous domains. The new solver is validated through comparisons with analytical solutions and, also, against established heat transfer solvers *chtMultiRegionFoam* and *compressibleInterFoam*. Further, a series of 2D and 3D case studies, including two-phase heat transfer in solid-free, static, or deformable porous media, highlights the solver's capacity to simulate complex flow dynamics and heat transport in systems involving high mobility ratios, viscous fingering, and fracture propagation. Our results establish the feasibility of incorporating thermal effects in simulations of a wide variety of energy geotechnics and environmental applications, including enhanced hydrocarbon recovery, soil remediation, and enhanced geothermal energy systems.

Plain Language Summary Understanding how heat, fluids, and mechanical forces interact in soils and rocks is important for addressing energy and environmental challenges, such as cleaning up contaminated land, enhancing groundwater recharge, and developing geothermal energy systems. These processes often occur in complex environments composed of both solid rock and open spaces. In this study, we developed a new computational model to better simulate how fluids move, heat is transferred, and rocks deform under realistic conditions. Unlike earlier models that assumed constant temperature, ours accounts for both heating and cooling effects. The tool can handle solid-free zones (such as fractures) as well as porous, flexible materials (such as clay-rich media). We validated the model by comparing it with known solutions and established simulation tools. We then applied it to several case studies involving the movement of hot or cold fluids through various types of underground materials. These examples demonstrate the model's ability to capture real-world behaviors, such as non-isothermal fluid fingering and fracture propagation. This work offers a powerful new way to study systems affected by fluid flow, mechanical deformation, and temperature gradients—helping engineers and scientists develop better strategies in the energy, environmental, and hydrological fields.

1. Introduction

Multiphase, multiphysics, and multiscale problems are central to many endeavors in geo-engineering, geo-energy, and environmental science, including hydrocarbon recovery, CO₂ sequestration, geothermal energy extraction, soil carbon storage, hydrology, and radioactive waste isolation (Bajestani et al., 2023; Hartley et al., 2021; Kirch et al., 2020; Vilarrasa & Rutqvist, 2017; Wang, de Hoop, et al., 2021; Wang, Chung, et al., 2021; Wang et al., 2023; Zheng & Bourg, 2023; Zheng et al., 2023). For example, in hydrologic systems, thermal effects and multiphase transport govern processes such as freeze-thaw cycles in soils and sediments, evaporation-induced desiccation cracking and associated groundwater recharge, and heat exchange in lakes and wetlands (Mohamed et al., 2021; Wong et al., 2017; Zhang et al., 2025). These applications involve interplay between multiple mobile phases (solid, liquid, gas) (Zheng & Espinoza, 2021b), diverse physical processes (fluid flow, heat transfer, chemical reactions, mechanical deformation) (Keyes et al., 2013), and a wide range of spatial and temporal scales—from microscale interactions within individual pores to the macroscale behavior of entire reservoirs or landscapes over years or decades (Horstemeyer, 2010). While significant strides have been made in

Writing – review & editing:
Xiaojin Zheng, Ian C. Bourg

modeling associated feedbacks, simultaneous representation of multiphase, multiphysics, and multiscale couplings remains challenging (Feng et al., 2022; Pal & Ramaswamy, 2023). A comprehensive framework that encompasses all important couplings remains essential to understand complex systems in the energy, environmental, and hydrologic sciences, as modeling only a subset of the relevant feedbacks poses a risk of misrepresenting system dynamics (Mehmani et al., 2013; Peters et al., 2019).

Efforts to integrate multiphase, multiphysics, and multiscale aspects into a coherent simulation framework present significant challenges. In subsurface systems, different phases—solid rock, water, gases, and organic fluids—interact through a variety of physical processes such as drainage and imbibition, dissolution and precipitation, creep and stress relaxation (Schott et al., 2009; Zheng & Espinoza, 2021a). A primary difficulty is that the different phases and processes are strongly interdependent. The resulting thermal, hydraulic, and mechanical (THM) couplings are driven by interactions at the pore scale, but these effects accumulate and manifest at the core scale or even at the reservoir scale (Sun et al., 2011). A second challenge is that different physical laws, such as chemical equilibrium, stress-strain, and fluid dynamics relations, can operate at vastly different temporal and spatial scales (Jebahi et al., 2016). For instance, at the microscale, multiphase interactions are dominated by molecular diffusion and capillary forces, while at the macroscale, these interactions are strongly modulated by viscous forces. The high-dimensional, nonlinear nature of coupled systems, with interactions between phase, physical, and spatial variables, increases the risk of numerical instability (Abbasi et al., 2023). Finally, thermal effects, though recognized as a component of THM couplings, are often viewed as secondary in comparison to hydraulic-mechanical interactions (Yin et al., 2010). In fact, temperature variations can drastically alter fluid properties and interfacial dynamics, influence chemical reactivity, and induce convective currents or thermosmosis (Dindoruk et al., 2020; Zagorščak et al., 2017). In high-temperature subsurface environments, thermal effects can lead to phase changes like water evaporation, resulting in density heterogeneities, rock shrinkage and cracking, and mechanical degradation (Bublik & Semin, 2022; Gautam et al., 2018; Manning & Aranovich, 2014). In hydrologic systems, temperature variations can drive critical feedbacks—for example, by altering evaporation rates that influence soil permeability or by affecting thermal gradients that govern hyporheic exchange (Heck et al., 2020; Wu et al., 2020).

The challenges outlined above become even more acute in complex porous media that contain both microporous domains and solid-free regions (e.g., fractured rock). Efforts to resolve these challenges have focused on improving the integration of multiscale physical processes through more efficient numerical methods and coupling schemes (Lv & Ekaterinaris, 2023; Radhakrishnan, 2021). Key approaches to capture the multiscale nature of fractured porous rock include direct numerical simulation (DNS), which fully resolves flow within the entire domain including individual micropores (Breugem & Boersma, 2005; Tryggvason et al., 2013; Wang, 2019); the DNS-Darcy approach, which applies Darcy's law to model fluid flow within microporous domains while resolving flow outside the porous domain via DNS, with a Beavers-Joseph (BJ) boundary condition between the two domains (Beavers & Joseph, 1967; Weishaupt et al., 2019); and the Darcy-Brinkman (DB) approach, which uses a single relation that asymptotically matches the Navier-Stokes equations in solid-free domains and Darcy's law within porous domains (Brinkman, 1949; Ochoa-Tapia & Whitaker, 1995). Despite these advances, limitations persist: DNS requires substantial computational resources, especially for systems with large disparities in length scales, while both the DNS-Darcy and DB approaches are generally constrained to single-phase flows in static porous media (Kang et al., 2019; Lesinigo et al., 2011; Singh, 2019).

A few years ago, a multiphase Darcy-Brinkman-Biot (DBB) approach was developed to simulate multiphase fluid flow in systems that contain both open spaces and deformable microporous domains (Carrillo & Bourg, 2019, 2021b; Carrillo et al., 2020). The resulting micro-continuum approach, derived using volume averaging theory (Soulaine et al., 2016; Whitaker, 1999), was successfully applied to model complex systems such as multiphase flow in fractured porous media, fracturing of porous solids by viscous or capillary stresses, and wave propagation in porous coastal barriers (Carrillo & Bourg, 2021a, 2021b). However, this multiscale DBB framework lacks the capability to model non-isothermal processes. To address this limitation, this study incorporates energy conservation equations into the multiscale DBB framework, creating a non-isothermal multiphase DBB framework. To the best of the authors' knowledge, this is the first model to simulate non-isothermal multiphase fluid flow in deformable porous media within a hybrid-scale framework (Figure 1).

The paper is organized as follows: Section 2 provides an overview of the governing equations and the theoretical foundation of the multiphase DBB framework. It then introduces the detailed derivation of the

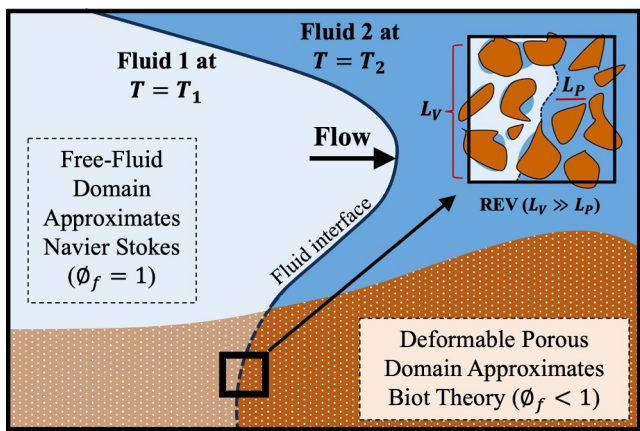


Figure 1. Conceptual illustration of the non-isothermal multiphase DBB framework. The system contains a deformable porous domain ($\Phi_f < 1$, where Φ_f is the porosity) in the lower half and a free-fluid domain ($\Phi_f = 1$) in the upper half. Two immiscible fluids, depicted as light blue and dark blue, are separated by an interface and exhibit distinct temperatures (T_1 and T_2). The representative elementary volume (REV) is the averaging scale for all equations, with L_p denoting the dimension of unresolved pores within microporous domains and L_v representing the computational grid size. Adapted from Carrillo and Bourg (2021b).

new energy conservation equation, followed by the numerical implementation of the resulting new solver, *hybridBiotThermalInterFoam*. To validate the solver's implementation, Section 3 presents a series of non-isothermal test cases, including comparisons with (a) an analytical solution for two-phase flow in porous media, (b) a numerical solution for single-phase flow in solid-free regions obtained using the established solver *chtMultiRegionFoam*, and (c) a numerical solution for two-phase flow obtained using the established solver *compressibleInterFoam*. Section 4 showcases five illustrative examples that highlight the model's versatility: warm water and supercritical CO₂ flooding in cool oil within a uniform rigid porous medium represented either at the Darcy scale or at the pore scale, warm water and glycerin injection into a deformable soft material, fracture development induced by fluid thermal expansion and contraction, as well as a three-dimensional case illustrative of an enhanced geothermal system. Section 5 concludes with a summary of the key findings and directions for future research. This new non-isothermal multiphase DBB framework integrates multiphase, multiphysics, and multiscale interactions into a comprehensive THM model, enabling predictions of complex phenomena in geo-energy, geotechnics, and a wide range of energy and environmental applications.

2. Methodology

2.1. Introduction to the DBB Framework

This section reviews the key governing equations of the multiphase DBB framework prior to the addition of the new energy conservation equation. This framework comprises five coupled equations governing the conservation of fluid mass (Equation 1), solid mass (Equation 2), fluid momentum (Equation 3), solid momentum (Equation 4), and fluid saturation (Equation 5) (Carrillo & Bourg, 2021b):

$$\frac{\partial \phi_f}{\partial t} + \nabla \cdot \mathbf{U}_f = 0 \quad (1)$$

$$\frac{\partial \phi_s}{\partial t} + \nabla \cdot \mathbf{U}_s = 0 \quad (2)$$

$$\frac{\partial \rho_f \mathbf{U}_f}{\partial t} + \nabla \cdot \left(\frac{\rho_f}{\phi_f} \mathbf{U}_f \mathbf{U}_f \right) = -\phi_f \nabla p + \phi_f \rho_f \mathbf{g} + \nabla \cdot \mathbf{S} - F_d (\mathbf{U}_f - \mathbf{U}_s) + \phi_f \mathbf{F}_c \quad (3)$$

$$\frac{\partial \rho_s \mathbf{U}_s}{\partial t} + \nabla \cdot \left(\frac{\rho_s}{\phi_s} \mathbf{U}_s \mathbf{U}_s \right) = -\phi_s \nabla (p + p_{sw}) + \phi_s \rho_s \mathbf{g} + \nabla \cdot \boldsymbol{\sigma} + F_d (\mathbf{U}_f - \mathbf{U}_s) - \phi_f \mathbf{F}_c \quad (4)$$

$$\frac{\partial \phi_f \alpha_w}{\partial t} + \nabla \cdot (\alpha_w \mathbf{U}_f) + \nabla \cdot \left(\phi_f \alpha_w \alpha_n \mathbf{U}_r \right) = 0 \quad (5)$$

In Equations 1–5, ϕ_f and ϕ_s represent the fluid and solid volume fractions ($\phi_f + \phi_s = 1$). \mathbf{U}_f and \mathbf{U}_s are the single-field fluid velocity and solid velocity, expressed as superficial phase-averaged properties: \mathbf{U}_f as a Darcy velocity for the fluid and \mathbf{U}_s as a “Darcy-like” velocity for the solid. \mathbf{U}_r is the relative velocity between the two immiscible fluids, defined as the difference between the intrinsic velocities of the wetting and non-wetting fluids. α_w and α_n are the saturations of the wetting and non-wetting fluids, respectively ($\alpha_w + \alpha_n = 1$). The single-field fluid density, ρ_f , is given by $\rho_f = \alpha_w \rho_w + \alpha_n \rho_n$, where ρ_w and ρ_n are the densities of the wetting and non-wetting fluids. ρ_s is the solid density, \mathbf{g} is the gravitational acceleration, and \mathbf{S} is the volume-averaged fluid viscous stress tensor. The terms F_d and \mathbf{F}_c determine fluid-solid momentum transfer due to viscous drag and capillary forces. Specifically, F_d depends on the solid permeability and single-field fluid viscosity, while \mathbf{F}_c is associated with the saturation gradient and capillary pressure-saturation relation. $\boldsymbol{\sigma}$ is the volume-averaged solid viscous stress tensor, parameterized to capture the viscoplastic rheology of many deformable Earth solids (Pradeep et al., 2024).

Spearman, 2017). The first term on the right side of Equation 4 incorporates p , the single-field fluid pressure, and p_{sw} , the swelling pressure of the microporous solid. This term reflects the influence of pore pressure and swelling pressure on the effective compressive stress, aligning with the definition of the Terzaghi stress tensor (Murad & Cushman, 2000). The closed-form expressions for the multiscale parameters, including F_c , F_d , and U_r , are defined uniquely for porous media and solid-free regions and can be found in previous studies (Carrillo & Bourg, 2019, 2021a, 2021b).

The set of partial differential equations outlined above effectively captures coupled inertial, viscous, capillary, interfacial, and gravitational forces. In systems that contain both porous and solid-free regions, the equations are applicable across all computational grid cells, eliminating the need to define separate meshes, domains, or complex interfacial boundary conditions. In solid-free regions, the set of Equations 1–5 asymptotically aligns with the multiphase Navier-Stokes equations as the drag force term vanishes; in microporous domains, it converges toward multiphase Darcy's law when viscous dissipation becomes negligible compared to the drag force exerted on the porous solid (Carrillo et al., 2020; Soulaine et al., 2019). This versatility is achieved by defining single-field parameters, which represent the volume-averaged material properties of the microporous medium at the scale of a computational grid element, based on the well-established volume-of-fluid (VOF) approach (Mohan & Tomar, 2024). The solution aligns with established treatments for systems containing both open spaces and microporous domains, such as the Beavers-Joseph boundary condition, provided two scale-separation conditions are met: (a) the computational grid elements must be significantly smaller than a macroscale defined by the dimensions of the free fluid and microporous domains, and (b) they must simultaneously be much larger than a microscale defined by the dimensions of the unresolved pores within the microporous domains (Neale & Nader, 1974; Nield, 2009).

2.2. Derivation of the Energy Conservation Equation

The energy conservation equation governs the distribution and transfer of thermal energy, making it a cornerstone in modeling non-isothermal problems (Bird et al., 2006). This equation typically includes terms for conductive heat transfer within the solid matrix and fluids, convective heat transfer due to fluid motion, the rate of local energy change, and contributions from energy sources or sinks (Kaviany, 2012). However, traditional formulations are generally derived for systems with static solids and a single length scale. In the subsequent paragraphs, we derive an energy conservation equation for multiphase fluid flow in deformable solids, employing single-field concepts within a hybrid-scale system. For a system involving three mobile phases (phase 1: wetting fluid; phase 2: non-wetting fluid; phase 3: solid), the conservation of internal energy, assuming no energy sources or sinks, can be expressed as:

$$\sum_{i=1}^3 \frac{\partial(f_i \rho_i c_{pi} T)}{\partial t} + \sum_{i=1}^3 \nabla \cdot (f_i \rho_i c_{pi} T \hat{U}_i) = \sum_{i=1}^3 \nabla \cdot (f_i \kappa_i \nabla T) \quad (6)$$

where T is absolute temperature, c_{pi} and κ_i are the heat capacity and thermal conductivity of phase i , f_i is the volume fraction of each phase ($f_w = \phi_f \alpha_w$, $f_n = \phi_f \alpha_n$, and $f_s = \phi_s$, with $\alpha_w + \alpha_n = 1$ and $\phi_f + \phi_s = 1$), and \hat{U}_i is the intrinsic velocity of phase i . For the wetting fluid, non-wetting fluid, and solid, the Darcy and intrinsic velocities are related through $U_w = \phi_f \alpha_w \hat{U}_w$, $U_n = \phi_f \alpha_n \hat{U}_n$, and $U_s = \phi_s \hat{U}_s$. The formulation in Equation 6 is consistent with using specific enthalpy to describe heat transport under the assumptions of incompressible or weakly compressible fluids, moderate pressure variations, and constant specific heat capacity. A similar approach has been widely adopted in previous porous media modeling studies (Bear, 1988; Lewis, 1998; Nield & Bejan, 2017).

The first term in Equation 6 can be rewritten in terms of the single-field fluid representation (as in Equations 1–5):

$$\sum_{i=1}^3 \frac{\partial(f_i \rho_i c_{pi} T)}{\partial t} = \frac{\partial[\phi_f (\rho c_p)_f T]}{\partial t} + \frac{\partial(\phi_s \rho_s c_{ps} T)}{\partial t} \quad (7)$$

where the single-field heat capacity of the fluid is defined as $(\rho c_p)_f = \alpha_w \rho_w c_{pw} + \alpha_n \rho_n c_{pn}$.

Similarly, the third term in Equation 6 can be rearranged as:

$$\sum_{i=1}^3 \nabla \cdot (f_i \kappa_i \nabla T) = \nabla \cdot [(\phi_f \kappa_f + \phi_s \kappa_s) \nabla T] \quad (8)$$

where the single-field fluid thermal conductivity is defined as $\kappa_f = \alpha_w \kappa_w + \alpha_n \kappa_n$.

The second term in Equation 6 can be expressed in terms of Darcy velocities. As described by Carrillo et al. (2020), the multiphase DBB framework uses the single-field fluid Darcy velocity $\mathbf{U}_f = \phi_f \alpha_w \hat{\mathbf{U}}_w + \phi_f \alpha_n \hat{\mathbf{U}}_n$ and the relative velocity $\mathbf{U}_r = \hat{\mathbf{U}}_w - \hat{\mathbf{U}}_n$. These relations can be combined to yield $\hat{\mathbf{U}}_w = \frac{\mathbf{U}_f}{\phi_f} + \alpha_n \mathbf{U}_r$ and $\hat{\mathbf{U}}_n = \frac{\mathbf{U}_f}{\phi_f} - \alpha_w \mathbf{U}_r$. These expressions are used to convert the second term in Equation 6 to the following form:

$$\sum_{i=1}^3 \nabla \cdot (f_i \rho_i c_{pi} T \hat{\mathbf{U}}_i) = \nabla \cdot [(\rho c_p)_f T \mathbf{U}_f + \alpha_w \alpha_n \phi_f (\rho_w c_{pw} - \rho_n c_{pn}) T \mathbf{U}_r + \rho_s c_{ps} T \mathbf{U}_s] \quad (9)$$

Finally, Equation 6 through 9 can be used to derive a new conservation equation for internal energy as a function of Darcy velocities and single-field fluid properties:

$$\begin{aligned} & \frac{\partial [\phi_f (\rho c_p)_f T]}{\partial t} \\ & + \frac{\partial (\phi_s \rho_s c_{ps} T)}{\partial t} + \nabla \cdot [(\rho c_p)_f T \mathbf{U}_f + \alpha_w \alpha_n \phi_f (\rho_w c_{pw} - \rho_n c_{pn}) T \mathbf{U}_r + \rho_s c_{ps} T \mathbf{U}_s] = \nabla \cdot [(\phi_f \kappa_f + \phi_s \kappa_s) \nabla T] \end{aligned} \quad (10)$$

Additional terms can be incorporated in Equations 6 and 10 to express the conservation of total energy, including the conversion between heat and mechanical energy. Similar to Equation 6, the conservation of mechanical energy for the sum of phases $i = 1$ through 3 is expressed as (Wendt, 2008):

$$\sum_{i=1}^3 \frac{\partial (f_i \rho_i K_i)}{\partial t} + \sum_{i=1}^3 \nabla \cdot (f_i \rho_i K_i \hat{\mathbf{U}}_i) = \sum_{i=1}^3 \nabla \cdot (f_i \boldsymbol{\sigma} \cdot \hat{\mathbf{U}}_i) + \sum_{i=1}^3 (f_i \rho_i \mathbf{g} \cdot \hat{\mathbf{U}}_i) \quad (11)$$

where $K_i = \frac{1}{2}(\hat{\mathbf{U}}_i)^2$ is the kinetic energy of phase i and $\boldsymbol{\sigma}$ is the total stress tensor. This formulation encompasses kinetic energy (first and second terms), strain energy (third term), and potential energy (fourth term). An equivalent expression can be written by decomposing $\boldsymbol{\sigma}$ into shear and normal components ($\boldsymbol{\sigma} = \boldsymbol{\tau} - p\mathbf{I}$):

$$\sum_{i=1}^3 \frac{\partial (f_i \rho_i K_i)}{\partial t} + \sum_{i=1}^3 \nabla \cdot (f_i \rho_i K_i \hat{\mathbf{U}}_i) = \sum_{i=1}^3 \nabla \cdot (f_i \boldsymbol{\tau} \cdot \hat{\mathbf{U}}_i) - \sum_{i=1}^3 \nabla \cdot (f_i p \hat{\mathbf{U}}_i) + \sum_{i=1}^3 (f_i \rho_i \mathbf{g} \cdot \hat{\mathbf{U}}_i) \quad (12)$$

Following the previous derivation process, the first term in Equation 12 can be expressed as $\sum_{i=1}^3 \frac{\partial (f_i \rho_i K_i)}{\partial t} = \frac{\partial (\phi_f \rho K_f)}{\partial t} + \frac{\partial (\phi_s \rho_s K_s)}{\partial t}$, where $(\phi_f \rho K_f) = \frac{1}{2} \left[\frac{\rho_f}{\phi_f} (\mathbf{U}_f)^2 + 2\alpha_w \alpha_n (\rho_w - \rho_n) \mathbf{U}_r \mathbf{U}_f + \phi_f \alpha_w \alpha_n (\rho_w \alpha_n + \rho_n \alpha_w) (\mathbf{U}_r)^2 \right]$; the second term is reformulated to substitute intrinsic phase velocities with Darcy velocities: $\sum_{i=1}^3 \nabla \cdot (f_i \rho_i K_i \hat{\mathbf{U}}_i) = \nabla \cdot \left\{ \frac{1}{2} \phi_f \left[\rho_f \left(\mathbf{U}_f / \phi_f \right)^3 + 3\alpha_w \alpha_n (\rho_w - \rho_n) \mathbf{U}_r \left(\mathbf{U}_f / \phi_f \right)^2 + 3\alpha_w \alpha_n \rho_f (\mathbf{U}_r)^2 \left(\mathbf{U}_f / \phi_f \right) + \alpha_w \alpha_n (\rho_w \alpha_n^2 - \rho_n \alpha_w^2) (\mathbf{U}_r)^3 \right] \right\} + \nabla \cdot \left[\frac{1}{2} \phi_s \rho_s (\hat{\mathbf{U}}_s)^3 \right]$; and the fourth term is written as: $-\sum_{i=1}^3 \nabla \cdot (f_i p \hat{\mathbf{U}}_i) = -\nabla \cdot (p \mathbf{U}_f + p \mathbf{U}_s)$. The third and fifth terms represent energy contribution from shear strain energy and potential energy, respectively, which are generally neglected due to their small magnitude. As a result, the mechanical energy conservation equation in Equation 12 becomes:

$$\begin{aligned} & \frac{\partial}{\partial t} \left\{ \phi_f \left[\rho_f \left(\mathbf{U}_f / \phi_f \right)^2 + 2\alpha_w \alpha_n (\rho_w - \rho_n) \mathbf{U}_r \left(\mathbf{U}_f / \phi_f \right) + \alpha_w \alpha_n (\rho_w \alpha_n + \rho_n \alpha_w) (\mathbf{U}_r)^2 \right] \right\} + \frac{\partial}{\partial t} \left[\frac{\rho_s}{\phi_s} (\mathbf{U}_s)^2 \right] \\ & + \nabla \cdot \left\{ \phi_f \left[\rho_f \left(\mathbf{U}_f / \phi_f \right)^3 + 3\alpha_w \alpha_n (\rho_w - \rho_n) \mathbf{U}_r \left(\mathbf{U}_f / \phi_f \right)^2 + 3\alpha_w \alpha_n \rho_f (\mathbf{U}_r)^2 \left(\mathbf{U}_f / \phi_f \right) + \alpha_w \alpha_n (\rho_w \alpha_n^2 - \rho_n \alpha_w^2) (\mathbf{U}_r)^3 \right] \right\} + \nabla \cdot \left[\frac{\rho_s}{\phi_s^2} (\mathbf{U}_s)^3 \right] + 2\nabla \cdot (p \mathbf{U}_f) + 2\nabla \cdot (p \mathbf{U}_s) = 0 \end{aligned} \quad (13)$$

The detailed derivation of Equation 13 is provided in the Supporting Information S1. Equation 13 captures the pressure work contributions, a key component of the enthalpy-based formulation, and is particularly important for highly compressible gases with pressure gradients. Finally, combining Equations 10 and 13 yields the total energy conservation equation, in which the total energy is the sum of internal and mechanical energy:

$$\begin{aligned} & \frac{\partial \left[\phi_f (\rho c_p)_f T \right]}{\partial t} + \frac{\partial \left(\phi_s \rho_s c_{ps} T \right)}{\partial t} + \nabla \cdot \left[(\rho c_p)_f T \mathbf{U}_f \right] + \nabla \cdot \left[\alpha_w \alpha_n \phi_f (\rho_w c_{pw} - \rho_n c_{pn}) T \mathbf{U}_r \right] \\ & + \nabla \cdot (\rho_s c_{ps} T \mathbf{U}_s) - \nabla \cdot \left[\left(\phi_f \kappa_f + \phi_s \kappa_s \right) \nabla T \right] + \left\{ \frac{\partial}{\partial t} \left[\phi_f \left(\mathbf{U}_f / \phi_f \right)^2 \right. \right. \\ & \left. \left. + 2\alpha_w \alpha_n (\rho_w - \rho_n) \mathbf{U}_r \left(\mathbf{U}_f / \phi_f \right) + \alpha_w \alpha_n (\rho_w \alpha_n + \rho_n \alpha_w) (\mathbf{U}_r)^2 \right] \right\} + \frac{\partial}{\partial t} \left[\frac{\rho_s}{\phi_s} (\mathbf{U}_s)^2 \right] \\ & + \nabla \cdot \left\{ \phi_f \left[\rho_f \left(\mathbf{U}_f / \phi_f \right)^3 + 3\alpha_w \alpha_n (\rho_w - \rho_n) \mathbf{U}_r \left(\mathbf{U}_f / \phi_f \right)^2 + 3\alpha_w \alpha_n \rho_f (\mathbf{U}_r)^2 \left(\mathbf{U}_f / \phi_f \right) \right. \right. \\ & \left. \left. + \alpha_w \alpha_n (\rho_w \alpha_n^2 - \rho_n \alpha_w^2) (\mathbf{U}_r)^3 \right] \right\} + \nabla \cdot \left[\frac{\rho_s}{\phi_s^2} (\mathbf{U}_s)^3 \right] + 2\nabla \cdot (p \mathbf{U}_f) + 2\nabla \cdot (p \mathbf{U}_s) \end{aligned} \quad (14)$$

The terms in Equation 14 represent various contributions to energy conservation. From left to right, the terms outside the curly brackets describe (a) the rate of change of the local internal energy in the fluid; (b) the rate of change of the local internal energy in the solid; (c–e) heat transfer due to single-field fluid flow, the relative velocity of wetting and non-wetting fluids, and solid displacement; and (f) thermal diffusion in the fluid and solid. Within the curly brackets, terms associated with mechanical energy include (g–i) the rate of change of the fluid's kinetic energy; (j) the rate of change of the solid's kinetic energy; (k–n) kinetic energy transfer due to fluid flow and the relative velocity of wetting and non-wetting fluids, (o) kinetic energy transfer due to solid displacement; and (p–q) pressure work terms in the fluid and solid. We note that the kinetic energy terms were found to have only minor effects in preliminary simulations of the example cases considered in this work. This is likely because kinetic energy is rapidly dissipated by viscous drag and the tortuous pore geometry, particularly under the Darcy-scale framework.

Equation 14 incorporates pressure-related flow work effects without explicitly reformulating the energy equation in terms of enthalpy. Formulations related to Equation 14 have been implemented in several OpenFOAM solvers—for example, *compressibleInterFoam*. However, these solvers either do not account for the presence of solids or are unable to model multiscale scenarios with coexisting porous and solid-free domains. To our knowledge, the total energy conservation equation presented in Equation 14 has not been previously derived in this form.

In summary, Equation 14 represents a total energy conservation consistent with the multiphase, multiscale DBB framework. In the following work, we combine Equation 14 with Equations 1–5 to represent multiphase, non-isothermal fluid flow in multiscale deformable porous media. Detailed discussions of the parameters in Equations 1–5 have been provided in earlier studies (Carrillo & Bourg, 2019, 2021a, 2021b).

2.3. Numerical Implementation

Several simplifications are applied in the implementation of Equation 14. First, phase saturation can exhibit steep gradients across sharp phase interfaces, resulting in large values of the relative velocity \mathbf{U}_r . The divergence of \mathbf{U}_r , which involves differences in fluxes between neighboring cell faces, is highly nonlinear and can be numerically unstable. To mitigate this, the term $\nabla \cdot \left[\phi_f \alpha_w \alpha_n T \mathbf{U}_r (\rho_w c_{pw} - \rho_n c_{pn}) \right]$ is approximated as

$\left[\phi_f \alpha_w \alpha_n (\rho_w c_{pw} - \rho_n c_{pn}) \mathbf{U}_r \right] \cdot \nabla T$, which represents the local heat exchange rate induced by the relative slip between the two phases along the temperature gradient. The numerically unstable contribution $T \cdot \left\{ \nabla \cdot \left[\phi_f \alpha_w \alpha_n (\rho_w c_{pw} - \rho_n c_{pn}) \mathbf{U}_r \right] \right\}$ that is omitted in this approximation is assumed negligible, a hypothesis supported by the validations presented in the following sections. Second, the volumetric heat capacity of the fluid is moved outside the divergence operator in the third term of Equation 14. The presence of $(\rho c_p)_f$ inside the divergence operator sometimes introduces noticeable computational artifacts, particularly where sharp gradients exist (e.g., at water-air interfaces), due to non-physical interpolation errors introduced when projecting cell-centered quantities to face values. Our treatment of this term as a cell-centered multiplier instead improves numerical stability. Finally, the term $\nabla \cdot (\rho_s c_{ps} T \mathbf{U}_s)$ is neglected under the assumption that the solid velocity \mathbf{U}_s is negligible compared to the fluid velocity \mathbf{U}_f . As observed in the following example cases, \mathbf{U}_s is two orders of magnitude smaller than \mathbf{U}_f , justifying this approximation. These simplifications are made to ensure computational efficiency and consistency with the test cases presented below, although further work is needed to evaluate their broader validity.

To couple temperature with other physical processes, the solver is modified to model fluid density and viscosity as temperature-dependent properties. For example, the density ρ_w ($\text{kg} \cdot \text{m}^{-3}$) and kinematic viscosity ν_w ($\text{m}^2 \cdot \text{s}^{-1}$) of liquid water are described by the relations $\rho_w = -3.53 \times 10^{-3}T^2 + 1.85T + 758.47$ and $\nu_w = 1.83 \times 10^{-10}T^2 - 1.31 \times 10^{-7}T + 2.36 \times 10^{-5}$, respectively, based on experimental results (Huber et al., 2009; Wagner & Prüß, 2002). For air, the density ρ_a ($\text{kg} \cdot \text{m}^{-3}$) is given by $\rho_a = \frac{p}{p_{ref}}(1.66 \times 10^{-5}T^2 - 1.38 \times 10^{-2}T + 3.83)$, based on the ideal gas law and experimental data (Hermann et al., 2009). The pressure-dependence coefficient p/p_{ref} is applied only to gases and is not used for liquids, which are treated as incompressible during the simulation. Additional temperature-dependent formulations for other fluid types can be readily incorporated within the solver's open-source framework.

Relative permeabilities and capillary pressure in porous domains are modeled using well-established Van Genuchten or Brooks-Corey constitutive relations (Brooks, 1965; van Genuchten, 1980). At each time step, relative permeability is updated to reflect the temperature dependence of dynamic viscosity. For example, the relative permeability of water is updated as $k_{rw} = k_{rw}^0 \frac{\mu_w}{\mu_w^0}$, where k_{rw}^0 and μ_w^0 are the relative permeability and dynamic viscosity of water at ambient temperature ($T_0 = 300$ K), respectively. Similarly, capillary pressure is updated to account for the temperature dependence of surface tension. More precisely, the surface tension between water and air is fitted from experimental results following the relationship $\sigma = \sigma_0 e^{b(T-T_0)}$ (Vargaftik et al., 1983). The T -dependence of the contact angle is assumed minimal, such that the capillary pressure difference between water and air can be approximated as $p_c = p_c^0 e^{b(T-T_0)}$, where $b = -2.47 \times 10^{-3} \text{ K}^{-1}$ and p_c^0 is the capillary pressure at ambient temperature. Absolute permeability is treated as isotropic and porosity-dependent, following the well-known Kozeny-Carman relation, $k = k_0 \phi_f^3 (1 - \phi_f)^{-2}$ (Rehman et al., 2024).

The solid's plasticity is captured using the Herschel-Bulkley model (Saasen & Ytrehus, 2020), where the solid undergoes viscous deformation only when local stresses exceed its yield stress. The yield stress and plastic viscosity of the solid are modeled as functions of the solid fraction, based on the Quemada fractal model (Quemada, 1977; Spearman, 2017). The swelling pressure p_{sw} is set to zero in this study. Detailed descriptions of the relative permeability, capillary pressure, and solid rheology models are provided in previous work (Carrillo & Bourg, 2021b).

We note that fluid densities ρ_w and ρ_n are not constants. To ensure mass conservation, the temperature-dependence of fluid density imposes the following modified form of Equation 1:

$$-\nabla \cdot \mathbf{U}_f = \frac{\partial \phi_f}{\partial t} + \left(\frac{\phi_f \alpha_w \partial \rho_w}{\rho_w} + \frac{\phi_f \alpha_n \partial \rho_n}{\rho_n} \right) + \mathbf{U}_f \left(\frac{\nabla \rho_w}{\rho_w} \alpha_w + \frac{\nabla \rho_n}{\rho_n} \alpha_n \right) + \mathbf{U}_r \phi_f \alpha_w \alpha_n \left(\frac{\nabla \rho_w}{\rho_w} - \frac{\nabla \rho_n}{\rho_n} \right) \quad (15)$$

The detailed derivation of Equation 15 is provided in the Supporting Information S1. As shown above, the thermal field is coupled to fluid flow through temperature-dependent fluid properties (e.g., density, viscosity) and to the mechanical field, indirectly, through temperature-dependent relative permeability and capillary pressure.

The governing equations are solved sequentially at each time step, beginning with the fluid mechanics equations followed by the solid mechanics equations. The energy conservation equation (Equation 14) is integrated within the PIMPLE (merged PISO–SIMPLE) loop to ensure velocity–pressure coupling in the single-field fluid. Iterative linear solvers are employed for each equation (e.g., GAMG for pressure and temperature, smoothSolver for velocities and solid displacements), with residual tolerances typically ranging from 10^{-5} to 10^{-8} . Numerical stability is maintained through adaptive time stepping with a target Courant number ≤ 0.5 , starting from $\Delta t = 10^{-7}$ s and automatically adjusting up to 0.1 s. The solver has been benchmarked on meshes of 0.5–1.0 million cells, decomposed into up to 96 subdomains, and executed efficiently on a standard HPC cluster. For example, in the hybrid-scale case described in Section 4.3, simulating 40 s of physical time required approximately 4 hr on 96 cores.

The previously developed multiphase DBB solver, *hybridBiotInterFoam* (Carrillo & Bourg, 2021b), was implemented in OpenFOAM 7, an open-source CFD platform. The platform utilizes C++ code and the Finite Volume Method to discretize and solve the partial differential equations. Building on *hybridBiotInterFoam*, the non-isothermal multiphase DBB model introduced here was incorporated into a new solver named *hybrid-BiotThermalInterFoam* (HBTIF). This new solver, along with its validation and application examples presented in this paper, is included in the open-source CFD package of the same name and can be accessed at <https://github.com/xiaojinz>.

3. Validation Examples

To validate the implementation of the *hybridBiotThermalInterFoam* solver, the following sections present several test cases. We begin by verifying the new solver with an analytical solution for non-isothermal two-phase flow in a uniform porous medium at the Darcy scale. Next, we perform a generic pore-scale simulation of non-isothermal single-phase flow in a rigid porous medium and compare the results with predictions from an established OpenFOAM solver, *chtMultiRegionFoam*. We then perform a Darcy-scale simulation of non-isothermal two-phase flow in a solid-free region and compare the results with another established OpenFOAM solver, *compressibleInterFoam*. The other core components of the multiphase DBB approach have been tested and validated for isothermal conditions in our previous work (Carrillo & Bourg, 2019, 2021b; Carrillo et al., 2020).

3.1. Darcy-Scale Validation for One-Dimensional Heat Transfer in a Porous Medium With Two Fluids

Multiphase heat transfer in porous media has been extensively studied in the field of energy geotechnics and environmental science (Kaviany, 2012). The heat transfer equation for a one-dimensional (1D) rigid porous medium with two fluids in a transient state, accounting for both conduction and convection, is generally expressed as (Carslaw & Jaeger, 1959; Kays et al., 2005):

$$\left(\phi_f \rho_f c_{pf} + \phi_s \rho_s c_{ps} \right) \frac{\partial T}{\partial t} + \rho_f c_{pf} U_f \frac{\partial T}{\partial x} = \left(\phi_f \kappa_f + \phi_s \kappa_s \right) \frac{\partial^2 T}{\partial x^2} \quad (16)$$

The assumptions underlying this equation are: (a) at any point in the medium, the solid and fluid phases are in local thermal equilibrium; (b) heat sources, sinks, and viscous heating are negligible; and (c) the properties before the derivatives are invariant in space and time. Although these assumptions may not hold true in complex scenarios, they enable the development of analytical solutions under simplified conditions.

In this validation case, a one-dimensional (1D) porous medium is initially saturated with 50% water and 50% air. A mixture of water and air with the same proportion, but with a high temperature (T_{in}), is injected at a velocity U_f through the inlet at $x = 0.1$ m (Figure 2a). With the boundary and initial conditions for temperature $T(x, 0) = T_0$ and $T(0, t) = T_{in}$, the heat at the inlet propagates through the porous medium as a function of time. Through application of the method of separation of variables or other appropriate transformations, the analytical solution to this problem can be derived using the complementary error function (Bird et al., 2006):

$$T(x, t) = T_0 + \frac{(T_{in} - T_0)}{2} \left[\operatorname{erfc} \left(\frac{x - vt}{2\sqrt{at}} \right) + \exp \left(\frac{vx}{a} \right) \operatorname{erfc} \left(\frac{x + vt}{2\sqrt{at}} \right) \right] \quad (17)$$

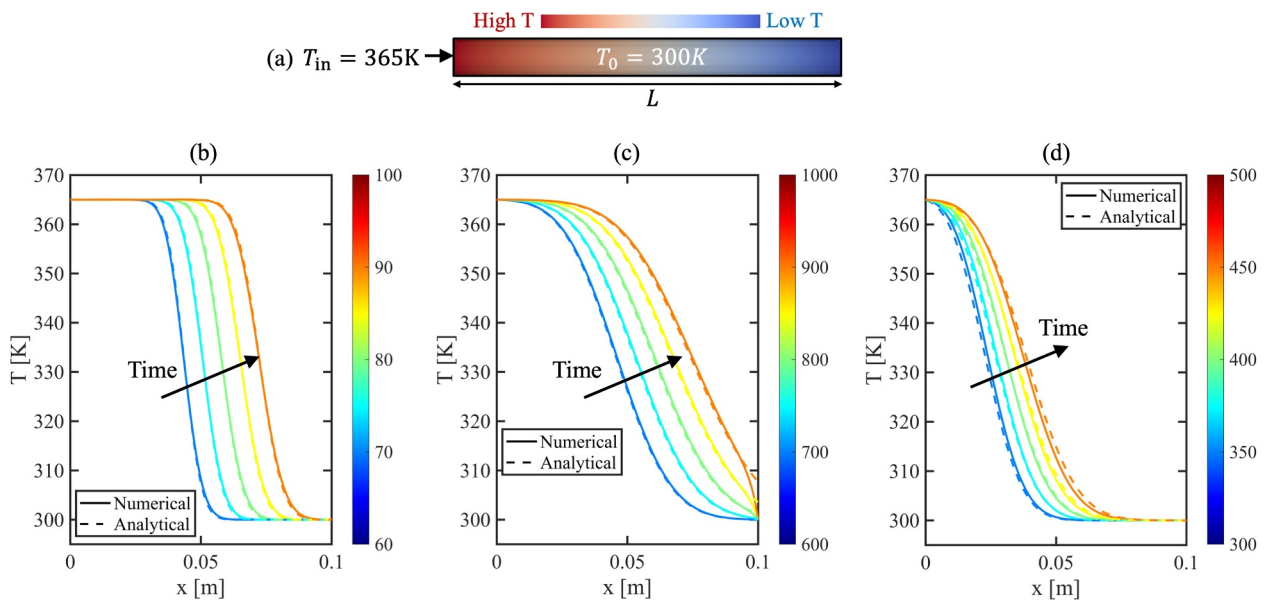


Figure 2. One-dimensional heat transfer in a porous medium containing water and air with uniform saturation ($\alpha_w = 0.5$) and with inflow of warm fluids at one boundary. (a) Simulation setup. (b and c) Temperature profiles generated by analytical solutions (dashed lines) and numerical predictions (solid lines) at $U_f = 1 \times 10^{-3}$ and $1 \times 10^{-4} \text{ m s}^{-1}$, respectively, with $\hat{U}_w = \hat{U}_n$. (d) Temperature profiles generated by analytical solutions (dashed lines) and numerical predictions (solid lines) at $\hat{U}_w = 8 \times 10^{-3} \text{ s}^{-1}$ and $\hat{U}_n = 4 \times 10^{-3} \text{ s}^{-1}$. Curves in panel (a) correspond to $t = 60, 70, 80, 90$, and 100 s . Curves in panel (c) correspond to $t = 600, 700, 800, 900$, and $1,000 \text{ s}$. Curves in panel (d) correspond to $t = 300, 350, 400, 450$, and 500 s .

where x is the horizontal coordinate, t is time, $v = \frac{\rho_f c_{pf} U_f}{\phi_f \rho_f c_{pf} + \phi_s \rho_s c_{ps}}$ represents the effective velocity of the thermal front, and $\alpha = \frac{\phi_f \kappa_f + \phi_s \kappa_s}{\phi_f \rho_f c_{pf} + \phi_s \rho_s c_{ps}}$ is the effective thermal diffusivity. The factor of $1/2$ accounts for the semi-infinite domain. The simulated porous medium has a length of 0.1 m and a porosity of 0.4. Other input parameters are listed in Table 1.

To validate the solver, we replicate the conditions of the analytical solution in a numerical simulation using *hybridBiotThermalInterFoam*. The fluid velocity is varied from 1×10^{-3} to $1 \times 10^{-4} \text{ m s}^{-1}$ to examine the impact of thermal convection versus conduction. The results shown in Figure 2 demonstrate that the numerical predictions closely match the analytical solution given by Equation 16. As expected, when fluid velocity is high (Figure 2b), convection dominates over conduction, and the temperature front advances rapidly along the flow direction, resulting in steeper temperature gradients. Conversely, at lower fluid velocities (Figure 2c), conduction prevails over convection, leading to more diffusive heat transport, with smoother temperature profiles and slower heat penetration (Ahsan, 2011). These results emphasize the role of fluid velocity in thermal conduction versus convection in modeling thermal processes.

Table 1
Input Parameters Used for the Analytical and Numerical Solutions Presented in Figure 2

Parameter	Value	Parameter	Value
$\kappa_{\text{water}} [\text{W}/(\text{m} \cdot \text{K})]$	0.6	$c_{p,\text{solid}} [\text{J}/(\text{kg} \cdot \text{K})]$	1,350
$\kappa_{\text{air}} [\text{W}/(\text{m} \cdot \text{K})]$	0.15	$c_{p,\text{air}} [\text{J}/(\text{kg} \cdot \text{K})]$	1,005
$\kappa_{\text{solid}} [\text{W}/(\text{m K})]$	1	$\alpha_w [-]$	0.5
$\rho_{\text{water}} [\text{kg}/\text{m}^3]$	996.16	$\phi_f [-]$	0.4 (in Figures 2b and 2c), 0.5 (in Figure 2d)
$\rho_{\text{air}} [\text{kg}/\text{m}^3]$	1.19	$L [\text{m}]$	0.1
$\rho_{\text{solid}} [\text{kg}/\text{m}^3]$	2,650	$T_0 [\text{K}]$	300
$c_{p,\text{water}} [\text{J}/(\text{kg} \cdot \text{K})]$	4,186	$T_{\text{in}} [\text{K}]$	365

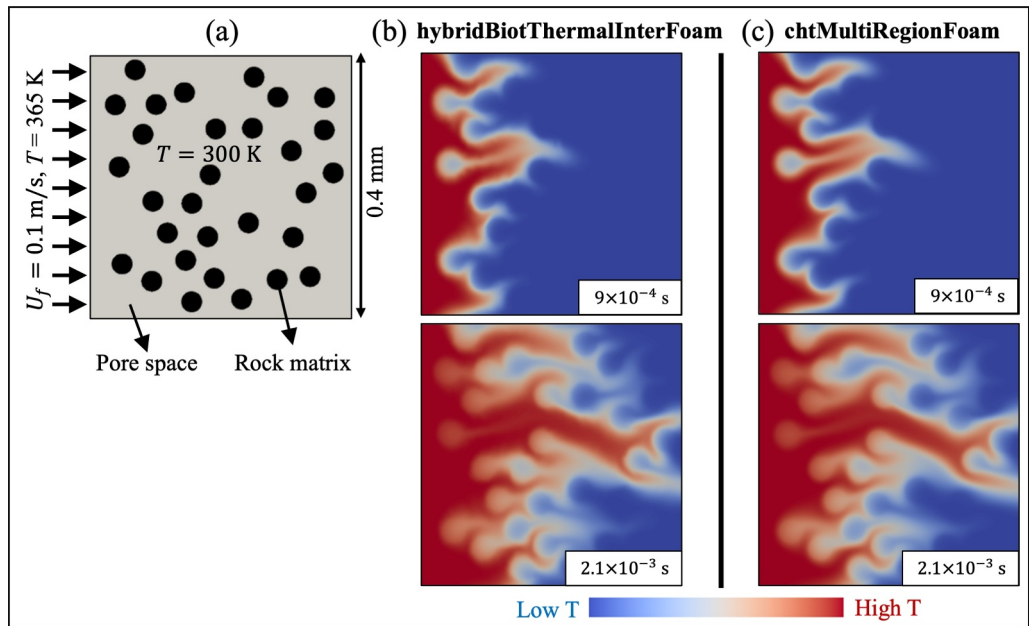


Figure 3. Temperature distributions predicted using *hybridBiotThermalInterFoam* and *chtMultiRegionFoam* during warm water injection in a water-saturated reservoir containing fixed solid beads. (a) Simulation setup. (b) Temperature distribution as a function of injection time with *hybridBiotThermalInterFoam*. (c) Temperature distribution as a function of injection time with *chtMultiRegionFoam*.

To validate the implementation of the relative velocity term (i.e., the fourth term in Equation 14), water and air are then injected at different intrinsic velocities (8×10^{-3} and $4 \times 10^{-3} \text{ m} \cdot \text{s}^{-1}$, respectively). The properties of the solids and fluids are the same as in the previous validation case, except that the porous medium now has a porosity of 0.4. In this setting, heat transfer associated with the relative motion between water and air is coupled with thermal convection, and Equation 15 becomes:

$$\left(\phi_f \rho_f c_{pf} + \phi_s \rho_s c_{ps} \right) \frac{\partial T}{\partial t} + \left[\phi_f \alpha_w \alpha_n (\rho_w c_{pw} - \rho_n c_{pn}) U_r + (\rho c_p)_f U_f \right] \frac{\partial T}{\partial x} = \left(\phi_f \kappa_f + \phi_s \kappa_s \right) \frac{\partial^2 T}{\partial x^2} \quad (18)$$

The analytical solution in Equation 16 is modified using $v = \frac{\phi_f \alpha_w \alpha_n (\rho_w c_{pw} - \rho_n c_{pn}) U_r + (\rho c_p)_f U_f}{\phi_f \rho_f c_{pf} + \phi_s \rho_s c_{ps}}$. For the system in Figure 2d, with $\rho_w c_{pw} \gg \rho_n c_{pn}$, $\alpha_w = 0.5$, and reported values of U_f and U_r , the U_r term contributes $1/4$ of the value of v and adequate treatment of this term is therefore required to correctly predict the propagation of the thermal front. As shown in Figure 2d, the simulation results are broadly consistent with the analytical solutions. These examples confirm the capability of the *hybridBiotThermalInterFoam* solver to capture multiphase heat transfer in 1D porous media.

3.2. Pore-Scale Validation for Heat Transfer in a Rigid Porous Medium With One Fluid

While analytical solutions, like the one presented earlier, offer useful approximations for simple systems, they become less accurate for complex systems with spatial heterogeneity. Therefore, after verifying heat transfer in a 1D porous medium, we now proceed to use an established numerical solver to evaluate the ability of *hybridBiotThermalInterFoam* to represent heat transfer during single-phase flow in a fully resolved two-dimensional (2D) pore geometry. In this validation case, warm water is injected into a cool water reservoir with randomly distributed beads. Hot water injection is commonly used in environmental engineering for soil and groundwater remediation, such as improving the efficiency of contaminant removal (Wang et al., 2022). Beads are often used as an analog for natural porous media like soil, sand, and rock, providing pore-scale insights into fluid flow dynamics, deformation under stress, heat and mass transfer, and more (Geistlinger & Zulfiqar, 2020).

As illustrated in Figure 3a, warm water at $T = 365 \text{ K}$ is injected into a water reservoir from the left boundary at a velocity of $0.1 \text{ m} \cdot \text{s}^{-1}$. The simulated domain measures $0.4 \text{ mm} \times 0.4 \text{ mm}$ in the horizontal plane with a thickness

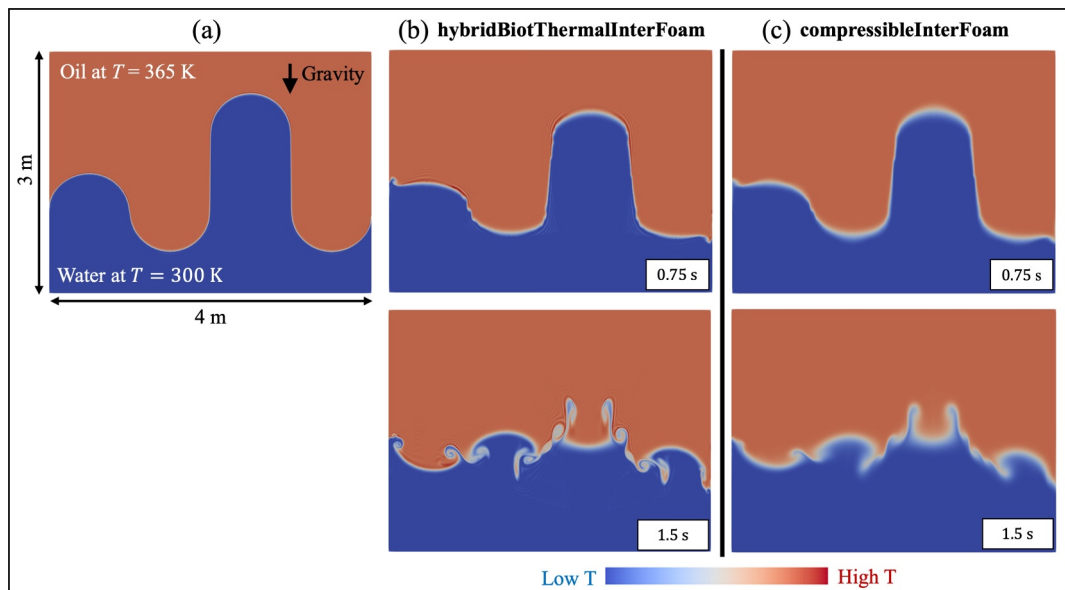


Figure 4. Temperature distributions predicted using *hybridBiotThermalInterFoam* and *compressibleInterFoam* for gravity-driven redistribution of immiscible cold water and warm oil. (a) Initial temperature field showing the initial distribution of water and oil. (b) Time-dependent temperature distribution predicted by *hybridBiotThermalInterFoam*. (c) Time-dependent temperature distribution predicted by *compressibleInterFoam*.

of 0.1 mm and is initially saturated with cool water at $T = 300\text{ K}$. The solid matrix is modeled as static beads. The simulation uses a zero-pressure boundary condition at the fluid outlet and a zero-gradient pressure boundary condition at the fluid inlet. This choice of pressure boundary conditions is consistent across all cases in this paper unless otherwise specified. Predicted temperature maps at various time steps are shown in Figure 3b.

To validate our solver, we run the same case with identical initial and boundary conditions using an existing pore-scale OpenFOAM solver, *chtMultiRegionFoam*. This solver, designed for conjugate heat transfer (CHT) problems, solves heat transfer in fluid and solid regions separately and is applicable only for cases with a single fluid and a static solid with fully-resolved pore structure (Khatibi, 2017). The results in Figure 3 show that simulations with *hybridBiotThermalInterFoam* and *chtMultiRegionFoam* produce nearly identical temperature fields. The predicted pressure distributions, presented in Figure S1 in Supporting Information S1, are likewise broadly consistent. This suggests that the simplifications made in the implementation of our solver are valid in cases such as those shown in Figure 3. The slight temperature difference at the fluid-solid interface can be attributed to differences in how the two solvers operate. In *chtMultiRegionFoam*, heat transfer in the fluid and solid phases is solved separately and then coupled at the fluid-solid interfaces, which requires more iterations to stabilize the coupled boundary conditions (Maes & Menke, 2022). In contrast, the new solver solves the temperature field for both phases using a single-field temperature equation. This example demonstrates that our solver can accurately simulate temperature distribution in complex porous systems with one fluid, producing results consistent with those obtained using the established *chtMultiRegionFoam* solver.

3.3. Darcy-Scale Validation for Heat Transfer in a Solid-Free Region With Two Fluids

After validating pore-scale 2D heat transfer during single-phase flow in a fully resolved porous medium, we extend the analysis to heat transfer involving two immiscible fluids. Specifically, we simulate gravity-driven two-phase flow, a phenomenon frequently encountered in energy recovery and environmental sustainability. As illustrated in Figure 4a, cool water at $T = 300\text{ K}$ is overlain by warm oil at $T = 365\text{ K}$. The simulated domain, measuring 3 m in height and 4 m in width, is maintained at atmospheric pressure. Water has a higher density ($996\text{ kg}\cdot\text{m}^{-3}$) and lower dynamic viscosity ($9.1 \times 10^{-4}\text{ Pa}\cdot\text{s}$) compared with oil ($842\text{ kg}\cdot\text{m}^{-3}$ and $0.011\text{ Pa}\cdot\text{s}$). After 1.5 s of simulation, gravitational forces cause the redistribution of water and oil, as shown in Figure 4b.

To validate the results, the same case was simulated using the established OpenFOAM solver *compressibleInterFoam*, which models two compressible, non-isothermal, and immiscible fluids using the Volume of Fluid

(VOF) method. Results demonstrate that our new solver produces consistent temperature distributions with *compressibleInterFoam*, as shown in Figure 4c. The discrepancies at the water–oil interface are likely due to the fact that *compressibleInterFoam* allows for a more diffuse phase saturation contrast across the fluid–fluid interface (as shown by the distribution of fluid saturation in Figure S2 in Supporting Information S1) and, also, that our solver applies volume-averaged thermal properties, whereas *compressibleInterFoam* computes phase-specific properties. This example validates the capability of the new solver to model multiphase heat transfer in solid-free regions and to simulate interactions between immiscible fluids, such as water, oil, and gas.

4. Illustrative Applications

After validating the implementation of our new non-isothermal solver both analytically (for Darcy-scale 1D two-phase fluid flow in a rigid porous medium) and numerically (for pore-scale 2D single-phase fluid flow in a rigid porous medium and for 2D two-phase fluid flow in a solid-free region), we now present several illustrative examples to highlight the features and capabilities of our model, including (a) Darcy-scale 2D multiphase fluid flow in a rigid porous medium, (b) pore-scale 2D multiphase fluid flow in a rigid porous medium, and (c) hybrid-scale 2D or 3D multiphase fluid flow in a deformable porous medium. The following example cases have a particular focus on fluid injection into porous geomaterials, a process used in a range of geotechnical and environmental engineering applications including enhanced oil recovery (EOR), hydraulic fracturing, contaminated soil remediation, and characterization of hydrogels and biomaterials (Alamooti et al., 2022; Bertsch et al., 2023; Tan et al., 2017).

4.1. Darcy Scale Simulation of Two-Dimensional Multiphase Heat Transfer

In the first example case, we simulate 2D two-phase fluid flow in a rigid homogeneous porous material. Water flooding and supercritical CO₂ (scCO₂) flooding are widely used EOR methods, where thermal effects can play a crucial role in influencing oil mobility and recovery efficiency (Kovscek, 2012; Mokheimer et al., 2018). In the simulated scenario, warm water or scCO₂ at $T = 365\text{ K}$ is injected at a flow rate of $6.28 \times 10^{-5}\text{ m}^3 \cdot \text{s}^{-1}$ from the center of a circular oil reservoir. The reservoir, initially at $T = 300\text{ K}$, has an outer radius of 0.5 m, an inner radius of 0.01 m, and a thickness of 0.1 m, and is modeled as a non-deformable porous matrix. The porosity follows a normal distribution with a mean of 0.4 and a standard deviation of 0.05. Permeability is modeled as a function of solid fraction using the Kozeny-Carman relation with $k_0 = 6.7 \times 10^{-12}\text{ m}^2$. Relative permeabilities and capillary pressure are calculated using the Brooks-Corey model.

After injection of warm water for 50 s, strong viscous fingering occurs due to the high mobility ratio between warm water and cool oil (Figure 5a). High mobility ratios generally lead to unstable displacement, as the lower-viscosity warm water moves faster and follows paths of least resistance, creating finger-like patterns in the cool oil. Supercritical CO₂, with a much lower viscosity than both oil and water, results in a larger viscosity contrast and stronger viscous fingering (Figure 5b) as shown in the distribution of the single-field fluid dynamic viscosity, defined as $\mu_f = \alpha_w \rho_w \nu_w + \alpha_n \rho_n \nu_n$. In summary, this simulation demonstrates the ability of our new solver to capture complex phenomena in non-isothermal two-phase flow within porous media, such as the influence of viscosity contrast on the stability of displacement fronts and the development of finger-like patterns in water and scCO₂ flooding.

4.2. Pore-Scale Simulation of Two-Dimensional Multiphase Heat Transfer

After presenting simulations of multiphase fluid flow in a uniform porous medium at the continuum scale, we now extend the study to a similar case where two fluids flow through a porous medium at the pore scale. In this scenario, we continue using bead packs to simulate loosely packed reservoir rocks and examine how injected fluids (water or scCO₂) displace oil in the presence of capillary and viscous forces and thermal fluxes. The size of the system is one-thousandth that of the setup in Figure 5 in each of the three spatial dimensions. Warm water or scCO₂ at $T = 365\text{ K}$ is injected at a flow rate of $6.28 \times 10^{-9}\text{ m}^3 \cdot \text{s}^{-1}$ from the center of a circular plate initially saturated with oil at $T = 300\text{ K}$. The circular plate contains 100 randomly distributed beads representing the rock matrix (Figure 6a). The beads have a radius of 0.02 mm and are fixed in place, without deformation or movement. The permeability, relative permeabilities, and capillary pressure conditions are modeled as in the previous section. As the simulation progresses, we monitor the development of temperature profiles and track the advance of the water- or scCO₂-oil interface (Figure 6b).

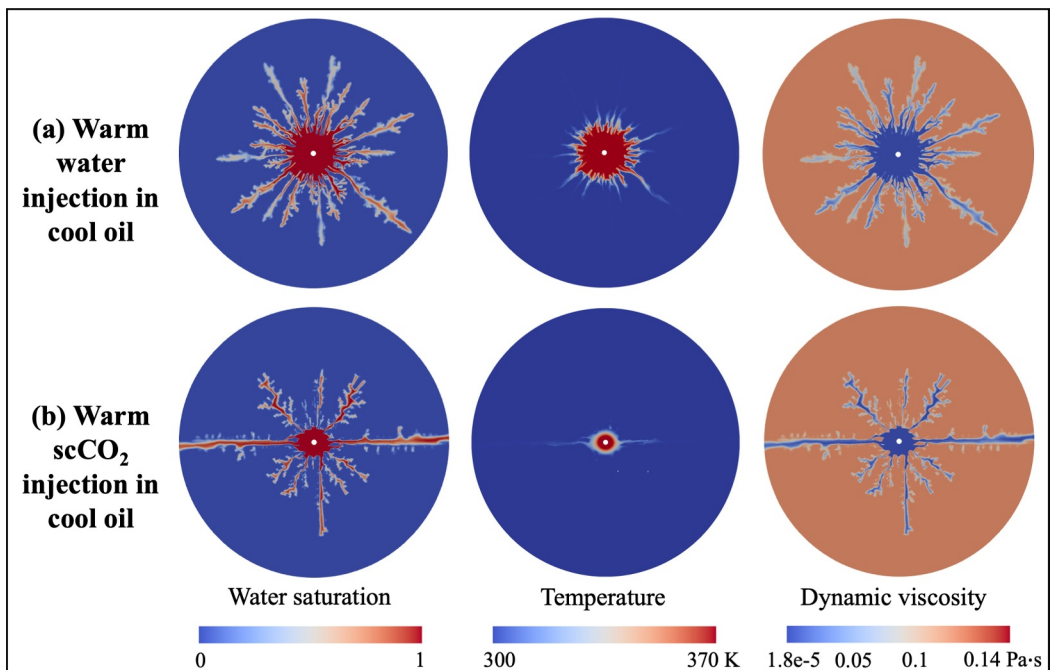


Figure 5. Injection of (a) warm water or (b) supercritical CO₂ (scCO₂) into a cool oil-saturated rigid porous medium. From left to right, panels show the distribution of water saturation, temperature, and single-field dynamic viscosity after 50 s of water or scCO₂ injection, respectively.

The results show consistent strong viscous fingering due to the viscosity difference between displacing and displaced fluids. As expected, scCO₂, with much lower viscosity and density than both oil and water, creates stronger viscous fingering and leads to early breakthrough (defined here as the displacing fluid reaching the plate boundary). This bypasses significant amounts of oil and reduces sweep efficiency. The distribution of fluid velocity after injecting scCO₂ for 0.002 s (Figure 6c) reveals a dominant flow channel within the oil phase. Over time, scCO₂ loses heat quickly to the surrounding cooler oil, leading to a rapid temperature drop, primarily due to scCO₂'s low specific heat capacity. Additionally, its lower thermal conductivity compared to water limits the

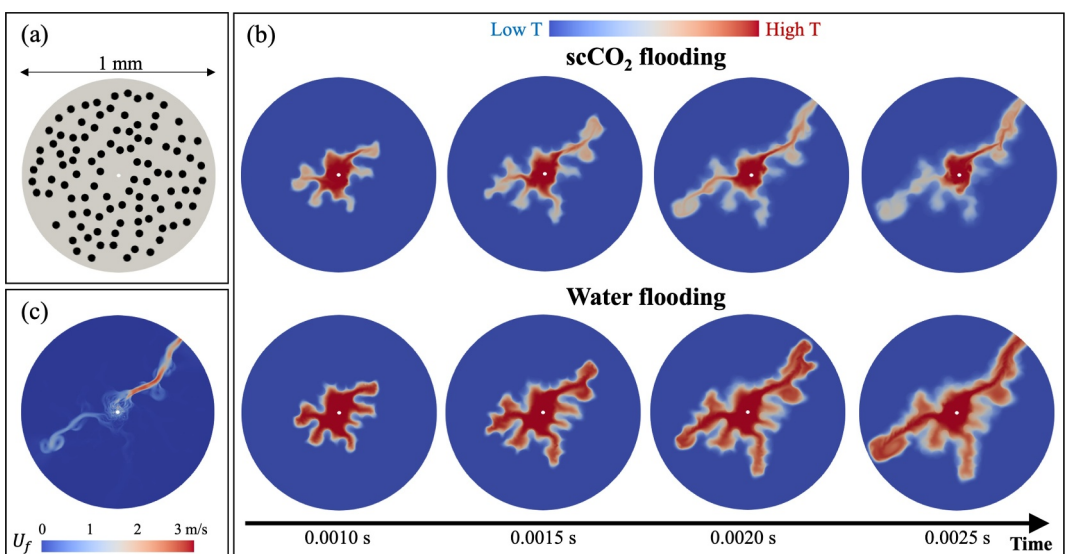


Figure 6. Injection of warm water and scCO₂ into a plate with cool oil-saturated, randomly distributed beads: (a) simulation setup; (b) temperature distribution as a function of injection time (upper panel: scCO₂ flooding; lower panel: water flooding); (c) distribution of single-field fluid velocity after 0.002 s of scCO₂ injection.

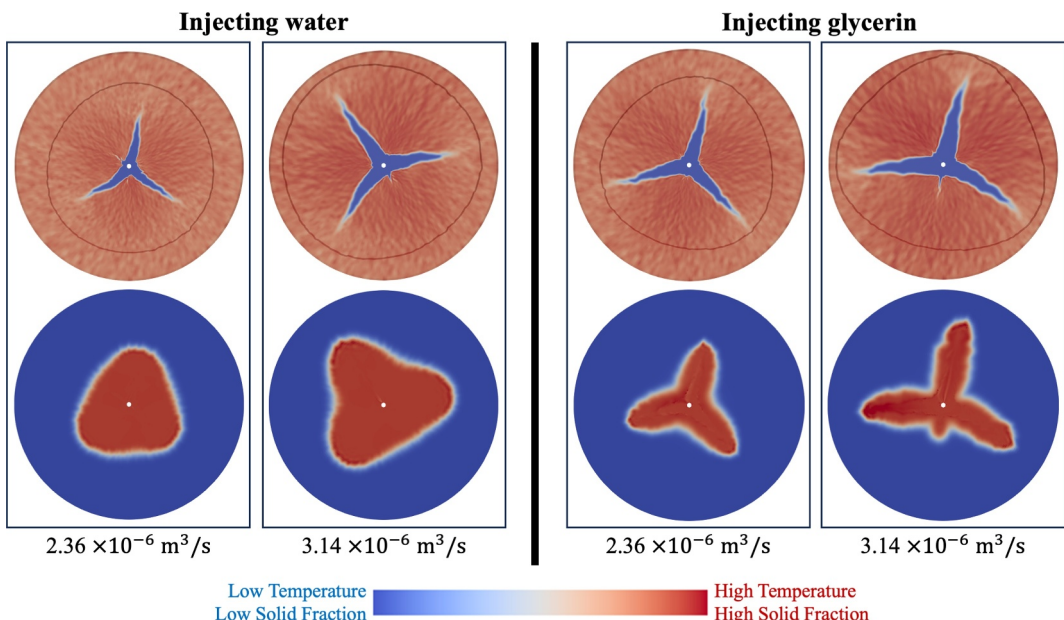


Figure 7. Simulation of water or glycerin injection into a dry clay-like material. The left and right panels show the results of water and glycerin injection at $t = 40$ s, respectively. In each panel, the upper and lower plots show the distribution of solid volume fraction and temperature, respectively. The black lines in the upper plots represent the advancing saturation front (defined as the contour where $\alpha_w = 0.95$). For each system, results are shown at two different flow rates from the circular hole at the center of the material.

distance over which heat spreads. In contrast, water, with its higher specific heat capacity, can store and retain more thermal energy. Coupled with its higher thermal conductivity, injected hot water transfers heat more effectively into the surrounding oil, enabling broader heat propagation (Figure 6b). These findings highlight the importance of considering thermal properties when optimizing displacement strategies in enhanced oil recovery, while demonstrating the solver's capability to model heat transfer in two-phase simulations of a fully resolved pore network.

4.3. Hybrid-Scale Simulation of Two-Dimensional Multiphase Heat Transfer in a Deformable Porous Medium: Viscous Fracturing

To evaluate the implementation of the solver in a hybrid-scale system, we investigate a scenario involving both porous and solid-free regions. The simulation in this section involves fluid injection into a soft material with the development of induced fractures and deformation (Figure 7). This hybrid-scale example was developed in a similar way in our previous work (Carrillo & Bourg, 2021a, 2021b) and is extended here to include thermal effects. Readers are referred to those publications for detailed discussions of the numerical strategy, solid mechanics, and mesh design. Warm water or glycerin at $T = 365$ K are injected into the center of a soft clay-like material at $T = 300$ K. The material is initially air-saturated, with an external radius of 0.125 m, an inner radius of 2.5 mm, and a thickness of 10 mm. The solid volume fraction follows a normal distribution with a mean of 0.6 and a standard deviation of 0.05. The “solid mechanics” module in the solver is activated to allow the solids to move. At the scale of the computational grid, permeability is modeled as a function of solid fraction using the Kozeny-Carman relation with $k_0 = 5 \times 10^{-11}$ m², and relative permeabilities and capillary pressure are calculated through the Van Genuchten model. The mechanics of the porous medium are represented using the Hershel-Bulkley-Quemada model (Quemada, 1977) with a yield stress $\tau_0 = 0.22$ m² · s⁻² for water injection and $\tau_0 = 10$ m² · s⁻² for glycerin injection. Different yield stress values are assigned to reflect the contrasting viscosities of water and glycerin and their respective roles in fracture initiation and propagation. The influence of yield stress on fracture development has been examined in detail in previous studies (Carrillo & Bourg, 2021a). Each simulation lasts 25 s. Each system is studied at two different flow rates (2.36×10^{-6} and 3.14×10^{-6} m³ s⁻¹) for comparison.

The fractured systems shown in Figure 7 require a hybrid scale representation, as the characteristic length scale of fractures ($\sim\text{cm}$) is several orders of magnitude larger than that of the pores within the porous matrix ($\sim 100 \text{ nm}$). The results show that the temperature front during water injection spreads further ahead of the fracture front, creating a more uniform and smoother heating profile. This is due to water's higher thermal conductivity and heat capacity compared to those of glycerin. In contrast, the injection of warm glycerin leads to more localized high-temperature zones. Additionally, a higher injection velocity promotes fracture propagation and convective heat transfer, causing the temperature distribution to become more concentrated along the fluid flow path, with less radial heat spreading into the surrounding medium. This simulation highlights the importance of considering both thermal and mechanical properties of materials for a better understanding of flow dynamics and heat transfer behavior in deformable solids. It also demonstrates the capability of this model to predict THM coupled processes in hybrid porous systems.

4.4. Hybrid-Scale Simulation of Two-Dimensional Multiphase Heat Transfer in a Deformable Porous Medium: Thermal Fracturing

We continue our illustration of the ability of the solver to represent porous and solid-free regions. However, instead of focusing on injection induced fractures, which are associated indirectly with temperature-dependent fluid properties, we now investigate thermally induced fractures triggered directly by fluid thermal expansion or contraction (Wibberley & Shimamoto, 2005). Specifically, we simulate a low-permeability compacted clay sample within a square domain of size $0.05 \times 0.05 \text{ m}$, characterized by a base permeability of $k_0 = 1 \times 10^{-17} \text{ m}^2$. The initial water saturation follows a normal distribution with a mean of 0.5 and a standard deviation of 0.05, with air as the complementary phase. The solid volume fraction is also normally distributed with a mean of 0.5 and a standard deviation of 0.05. Solid mechanics are described using the Herschel–Bulkley–Quemada model, with a yield stress of $\tau_0 = 1.2 \text{ m}^2 \cdot \text{s}^{-2}$. A cyclic thermal loading is applied at the left boundary: the temperature at this boundary is increased linearly from 300 to 350 K over the first 2,500 s, then decreased back to 300 K over the next 2,500 s, and held at 300 K for the final 1,000 s, yielding a total simulation time of 6,000 s. The right boundary is open to flow with pressure fixed at atmospheric conditions, while the remaining three boundaries are impermeable. The solid is constrained from moving at all boundaries, mimicking confinement by a container or surrounding rock.

The results in Figures 8a–8c show that as temperature increases from 300 to 350 K, fluid thermal expansion drives the development of fractures, with the most pronounced fracturing observed at the peak temperature of 350 K. Upon cooling from 350 back to 300 K, the thermally induced fractures begin to close (Figure 8d), while simultaneously, fluid thermal contraction initiates new fractures (Figure 8e), which continue to develop during further cooling (Figure 8f). Notably, in this case no additional external drivers (e.g., injection as in the previous section) are applied. This highlights the solver's ability to capture directly thermally driven fracture processes in low-permeability ductile barriers relevant, for example, to radioactive waste repositories. The findings underscore the important impact of temperature variations on material integrity and suggest potential guidelines for preventing thermal damage and implementing precautionary strategies.

4.5. Hybrid-Scale Simulation of Three-Dimensional Multiphase Heat Transfer in a Deformable Porous Medium

After testing the model in 2D cases, we now proceed to present an illustrative example of a three-dimensional (3D) scenario. In this case, we leverage the ability of *hybridThermalBiotInterFoam* to simulate multiphase heat transfer in hybrid-scale deformable porous media, with potential applications in an enhanced geothermal system (EGS), as shown in Figure 9. The EGS process involves creating fractures in porous rocks to enhance permeability, allowing fluids to circulate and extract heat from dry hot rocks. Detailed understanding of thermal effects and fracture development is crucial for estimating reservoir performance and optimizing energy output. This inherently represents a multiphase, multiscale, and multiphysics problem, as the injection of cooler fluids into hot rocks induces water-rock heat transfer, formation pressurization, fracture propagation, and permeability alteration (Rathnaweera et al., 2020).

In this case, cool water at $T = 300 \text{ K}$ is injected from the perforation interval at the center of a cylindrical reservoir. The simulated reservoir has an outer radius of 0.125 m, an inner radius of 2.5 mm, and a height of 0.25 m (Figure 9a). The reservoir has an initial mean porosity of $\phi_f = 0.5$ (with a standard deviation of 0.05),

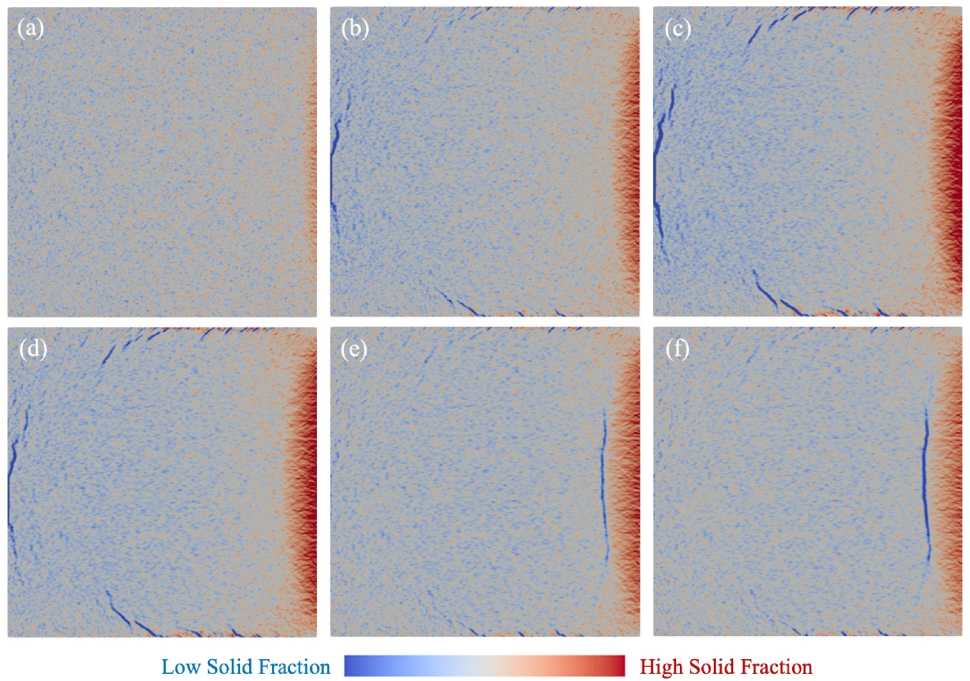


Figure 8. Development of thermally induced fractures in a bentonite barrier for high-level radioactive waste isolation. The temperature increases linearly from 300 to 350 K during 0–2,500 s, decreases back to 300 K over 2,500–5,000 s, and remains at 300 K from 5,000 to 6,000 s. Subplots (a–f) show solid volume fraction distributions at $t = 1,000, 2,000, 2,500, 4,000, 5,000$, and 6,000 s, respectively. Subplots (a–c) illustrate fracture development due to thermal expansion, while subplots (d–f) depict fracture closure and new fracture initiation caused by thermal contraction.

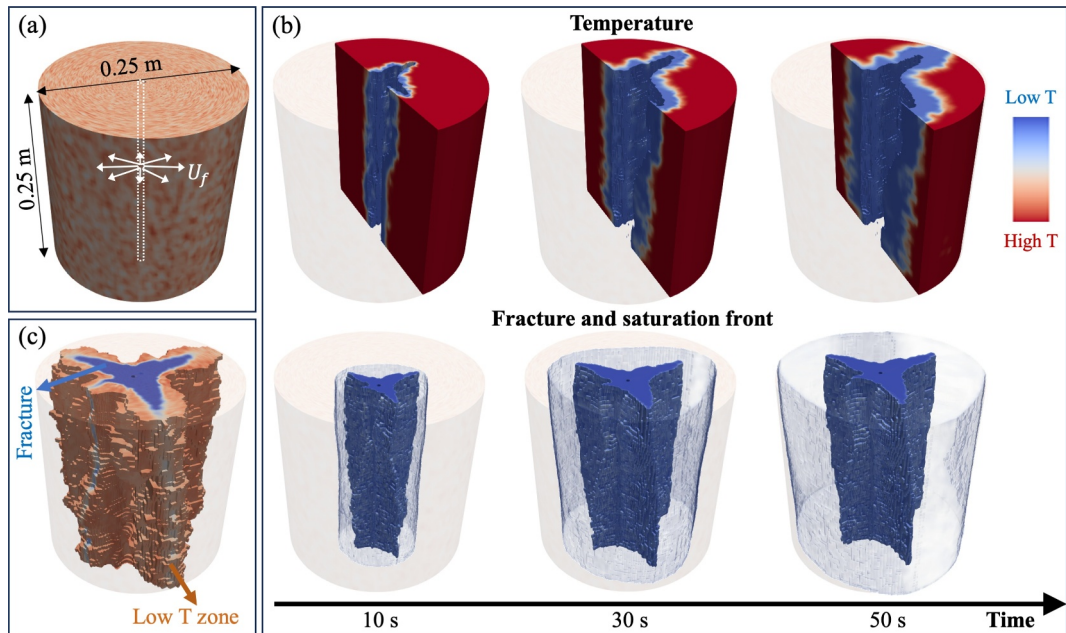


Figure 9. Simulated injection of cool water into a dry hot formation designed to mimic an enhanced geothermal system: (a) simulation setup, where cool water is injected from the perforation column at the center of the simulated cylindrical formation; (b) distribution of temperature, three-dimensional fracture geometry, and spatial saturation front ($S_w > 0.95$) as a function of time (upper panel: temperature; lower panel: fracture and saturation front); (c) distribution of the low-temperature zone ($T < 310$ K) after 50 s of cool water injection. In (a) and (c), color represents solid fraction from 0 (blue) to 1 (red).

with the pore space saturated by 85% water and 15% air. The reservoir, initially at a warm temperature of $T = 365$ K, is modeled as a plastic material with a yield stress of $\tau_0 = 1 \text{ m}^2 \cdot \text{s}^{-2}$. The relative permeabilities and capillary pressure are calculated through the Brooks-Corey model. Injection occurs over 50 s at a flow rate of $1.18 \times 10^{-4} \text{ m}^3 \cdot \text{s}^{-1}$. The resulting temperature field (across both injection-induced fractures and porous regions) is shown in Figure 9b as a function of time. The induced fracture propagates from the perforation column, accompanied by the development of a low-temperature zone ($T < 310$ K) around it. Over the injection period, the low-temperature zone grows anisotropically due to the formation's heterogeneity and approaches the boundary of the simulated reservoir (Figure 9c). The saturation front ($S_w > 0.95$) advances faster than the low-temperature zone, nearly reaching the entire formation by the end of the 50 s.

This observed evolution of fracture propagation, temperature distribution, and saturation front can provide valuable insights into the coupled physics involved in enhanced geothermal systems. This illustrative example demonstrates that our modeling framework is versatile and can be applied to a wide range of geo-engineering systems, opening new possibilities for simulating THM coupled engineering problems. However, to better mimic realistic rock physics, further efforts are needed to refine the constitutive and parametric relations in the solver, including those governing permeability, capillarity, and solid mechanics within volume-averaged porous regions (Carrillo & Bourg, 2021a, 2021b).

5. Conclusions

This study introduces the development and implementation of a non-isothermal multiphase Darcy-Brinkman-Biot (DBB) framework that integrates thermal, hydraulic, and mechanical (THM) processes to model complex geo-engineering and geoscience problems. The new framework advances the existing multiphase DBB model by incorporating an energy conservation equation, enabling the simulation of non-isothermal conditions in pore, Darcy, or hybrid scale systems containing deformable porous domains and solid-free regions. The model's numeric and algorithmic development was implemented in *hybridBiotThermalInterFoam*, an open-source package based on OpenFOAM, which is freely accessible. The solver was validated through a series of test cases involving both analytical and numerical simulations. These validations demonstrated the solver's capacity to accurately simulate multiphase flow in porous media and solid-free regions under non-isothermal conditions. The model's versatility was further highlighted through applications to warm water or scCO₂ flooding in oil reservoirs, fracture propagation induced by water or glycerin injection, fracture development triggered by fluid thermal expansion and contraction, and coupled physics in enhanced geothermal systems. These examples showcase the model's ability to simulate a broad range of physical processes across multiple scales, from the pore level to the reservoir scale, from single-phase to multiphase flow, and from static to viscoplastic porous media.

Other advanced THM modeling approaches, such as phase-field models and extended finite element methods, are highly effective at capturing complex fracture behaviors. However, they typically involve significant computational overhead or mesh complexity, and many are limited to single-phase flow (Mollaali et al., 2023; Yu et al., 2021). Commercial finite element platforms like COMSOL Multiphysics offer intuitive model setup and built-in multiphysics coupling, but they are constrained by their proprietary nature, limited scalability for large-scale 3D problems, and weaker support for temperature-dependent multiphase transport (Souley et al., 2024). In contrast, our solver, *hybridBiotThermalInterFoam*, is built on the widely adopted open-source OpenFOAM platform and offers flexibility and extensibility for simulating complex multiphase thermal transport (Jasak, 2009). It benefits from high-performance parallel computing and leverages the Volume-of-Fluid (VOF) method to capture immiscible two-phase flow. Future work will examine the solver's computational efficiency for large-scale multiphase thermal transport simulations. Moreover, the solver accounts for temperature-dependent variations in viscosity, density, and interfacial tension, while also conserving the mass of fluids with temperature-dependent density. It also supports seamless modeling across both Darcy-scale and pore-scale regimes, enabling multiscale simulations that are not addressed by the aforementioned solvers. The development of this non-isothermal multiphase DBB framework provides a powerful tool for understanding multiphase, multiphysics, and multiscale coupled phenomena, particularly those with complex thermal dynamics. These coupled effects are critical in a wide range of energy geotechnics, hydrology, Earth science, and environmental engineering applications, including enhanced oil recovery, hydraulic fracturing, enhanced geothermal energy, radioactive waste isolation, cohesive sediment transport, sustainable groundwater recharge, and seasonal thermal energy storage.

Future research is required to refine the constitutive relationships within the solver, especially for highly heterogeneous media and extreme environments with large deformations and strong thermal fluxes (Wang, de Hoop, et al., 2021; Wang, Chung, et al., 2021). For example, the Darcy-scale rheological properties of ductile porous geomaterials were modeled here as invariant with saturation or temperature due to a lack of experimental characterization. Similarly, the impact of temperature on capillary pressure was assumed to derive entirely from the temperature-dependence of fluid-fluid interfacial tension, due to limited knowledge of the impact of temperature on rock wettability (Pham et al., 2023). Another opportunity for future research is the incorporation of direct couplings between different fluxes, such as thermo-osmosis (i.e., flow of solution driven by a gradient in temperature), which are often neglected because of a lack of fundamental understanding (Chen et al., 2021). The implementation of additional modules may be needed to accommodate the complex coupling between fluid flow and solid mechanics, such as phase changes (e.g., freezing or evaporation) (Qiao et al., 2025), solute transport (Chen et al., 2023), the brittle mechanics of hard rocks (vs. the ductile mechanics represented here), the swelling pressure of compacted clay, and chemical reactions (e.g., mineral dissolution and precipitation). Lastly, future work will focus on experimental validation through laboratory-scale heated flow-through tests (Zhao & Brown, 1992) and, where possible, benchmarking against other multiscale coupled THM solvers. Such efforts will enable a more rigorous evaluation of the model's applicability under realistic conditions.

Conflict of Interest

The authors declare no conflicts of interest relevant to this study.

Data Availability Statement

The non-isothermal multiphase DBB model developed in this study has been implemented in a new solver, *hybridBiotThermalInterFoam*. This solver—along with its validation cases and application examples—is available as part of an open-source CFD package under the same name, accessible at <https://github.com/xiaojinz>.

Acknowledgments

This research was supported by the U.S. Department of Energy, Office of Nuclear Energy, under Award DE-NE0009323 and by the U.S. Department of Energy, Office of Science, Office of Basic Energy Science, under Award DE-SC0018419. Additional support was provided by Princeton University. OpenFOAM simulations were performed using computational resources managed and supported by Princeton Research Computing, a consortium of groups including the Princeton Institute for Computational Science and Engineering (PICSciE) and the Office of Information Technology's High Performance Computing Center and Visualization Laboratory at Princeton University.

References

- Abbasi, A., Kambali, P. N., & Nataraj, C. (2023). Hybrid modeling of a multidimensional coupled nonlinear system with integration of Hamiltonian mechanics. *Nonlinear Dynamics*, 111(16), 15011–15022. <https://doi.org/10.1007/s11071-023-08618-0>
- Ahsan, A. (Ed.). (2011). *Convection and conduction heat transfer*. InTechOpen.
- Alamooti, A., Colombano, S., Omirbekov, S., Ahmadi, A., Lion, F., & Davarzani, H. (2022). Influence of the injection of densified polymer suspension on the efficiency of DNAPL displacement in contaminated saturated soils. *Journal of Hazardous Materials*, 440, 129702. <https://doi.org/10.1016/j.jhazmat.2022.129702>
- Bajestani, M. S., Nasir, O., & Oh, W. T. (2023). Properties of bentonite-based sealing materials during hydration. *Minerals*, 13(11), 1412. <https://doi.org/10.3390/min13111412>
- Bear, J. (1988). *Dynamics of fluids in porous media*. Dover Publications.
- Beavers, G. S., & Joseph, D. D. (1967). Boundary conditions at a naturally permeable wall. *Journal of Fluid Mechanics*, 30(1), 197–207. <https://doi.org/10.1017/S0022112067001375>
- Bertsch, P., Diba, M., Mooney, D. J., & Leeuwenburgh, S. C. G. (2023). Self-healing injectable hydrogels for tissue regeneration. *Chemical Reviews*, 123(2), 834–873. <https://doi.org/10.1021/acs.chemrev.2c00179>
- Bird, R. B., Stewart, W. E., & Lightfoot, E. N. (2006). *Transport phenomena*. John Wiley & Sons.
- Breugem, W. P., & Boersma, B. J. (2005). Direct numerical simulations of turbulent flow over a permeable wall using a direct and a continuum approach. *Physics of Fluids*, 17(2), 025103. <https://doi.org/10.1063/1.1835771>
- Brinkman, H. C. (1949). A calculation of the viscous force exerted by a flowing fluid on a dense swarm of particles. *Flow, Turbulence and Combustion*, 1(1), 27–34. <https://doi.org/10.1007/BF02120313>
- Brooks, R. H. (1965). *Hydraulic properties of porous media* (Ph.D. dissertation). Colorado State University.
- Bublik, S., & Semin, M. (2022). Numerical simulation of phase transitions in porous media with three-phase flows considering steam injection into the oil reservoir. *Computation*, 10(12), 205. <https://doi.org/10.3390/computation10120205>
- Carrillo, F. J., & Bourg, I. C. (2019). A Darcy-Brinkman-Biot approach to modeling the hydrology and mechanics of porous media containing macropores and deformable microporous regions. *Water Resources Research*, 55(10), 8096–8121. <https://doi.org/10.1029/2019WR024712>
- Carrillo, F. J., & Bourg, I. C. (2021a). Capillary and viscous fracturing during drainage in porous media. *Physical Review E*, 103(6), 063106. <https://doi.org/10.1103/PhysRevE.103.063106>
- Carrillo, F. J., & Bourg, I. C. (2021b). Modeling multiphase flow within and around deformable porous materials: A Darcy-Brinkman-Biot approach. *Water Resources Research*, 57(2), e2020WR028734. <https://doi.org/10.1029/2020WR028734>
- Carrillo, F. J., Bourg, I. C., & Soulaine, C. (2020). Multiphase flow modeling in multiscale porous media: An open-source micro-continuum approach. *Journal of Computational Physics*, X(8), 100073. <https://doi.org/10.1016/j.jcp.2020.100073>
- Carslaw, H. S., & Jaeger, J. C. (1959). *Conduction of heat in solids*. Clarendon Press.
- Chen, H., Zhang, Z., Jin, G., Tang, H., Zhang, S., & Zhang, Q. (2023). Effects of periodic fluctuation of water level on solute transport in seasonal lakes in Poyang floodplain system. *Water Resources Research*, 59(12), e2023WR034739. <https://doi.org/10.1029/2023WR034739>
- Chen, W. Q., Sedighi, M., & Jivkov, A. P. (2021). Thermo-osmosis in hydrophilic nanochannels: Mechanism and size effect. *Nanoscale*, 13(3), 1696–1716. <https://doi.org/10.1039/D0NR06687G>

- Dindoruk, B., Ratnakar, R., & He, J. (2020). Review of recent advances in petroleum fluid properties and their representation. *Journal of Natural Gas Science and Engineering*, 83, 103541. <https://doi.org/10.1016/j.jngse.2020.103541>
- Feng, D., Chen, Z., Wu, K., Li, J., Dong, X., Peng, Y., et al. (2022). A comprehensive review on the flow behaviour in shale gas reservoirs: Multi-scale, multi-phase, and multi-physics. *Canadian Journal of Chemical Engineering*, 100(11), 3084–3122. <https://doi.org/10.1002/cjce.24439>
- Gautam, P. K., Verma, A. K., Jha, M. K., Sharma, P., & Singh, T. N. (2018). Effect of high temperature on physical and mechanical properties of Jaloré granite. *Journal of Applied Geophysics*, 159, 460–474. <https://doi.org/10.1016/j.jappgeo.2018.07.018>
- Geistlinger, H., & Zulfiqar, B. (2020). The impact of wettability and surface roughness on fluid displacement and capillary trapping in 2-D and 3-D porous media: 1. Wettability-controlled phase transition of trapping efficiency in glass beads packs. *Water Resources Research*, 56(10), e2019WR026826. <https://doi.org/10.1029/2019WR026826>
- Hartley, I. P., Hill, T. C., Chadburn, S. E., & Hugelius, G. (2021). Temperature effects on carbon storage are controlled by soil stabilisation capacities. *Nature Communications*, 12(1), 6713. <https://doi.org/10.1038/s41467-021-27101-1>
- Heck, K., Coltman, E., Schneider, J., & Helmig, R. (2020). Influence of radiation on evaporation rates: A numerical analysis. *Water Resources Research*, 56(10), e2020WR027332. <https://doi.org/10.1029/2020WR027332>
- Herrmann, S., Kretzschmar, H.-J., & Gatley, D. P. (2009). Thermodynamic properties of real moist air, dry air, steam, water, and ice (RP-1485). *HVAC & R Research*, 15(5), 961–986. <https://doi.org/10.1080/10789669.2009.10390874>
- Horstemeyer, M. F. (2010). Multiscale modeling: A review. In J. Leszczynski & M. K. Shukla (Eds.), *Practical aspects of computational chemistry: Methods, concepts and applications* (pp. 87–135). Springer Netherlands. https://doi.org/10.1007/978-90-481-2687-3_4
- Huber, M. L., Perkins, R. A., Laesecke, A., Friend, D. G., Sengers, J. V., Assael, M. J., et al. (2009). New international formulation for the viscosity of H₂O. *Journal of Physical and Chemical Reference Data*, 38(2), 101–125. <https://doi.org/10.1063/1.3088050>
- Jasak, H. (2009). OpenFOAM: Open source CFD in research and industry. *International Journal of Naval Architecture and Ocean Engineering*, 1(2), 89–94. <https://doi.org/10.2478/IJNAOE-2013-0011>
- Jebahi, M., Dau, F., Charles, J.-L., & Iordanoff, I. (2016). Multiscale modeling of complex dynamic problems: An overview and recent developments. *Archives of Computational Methods in Engineering*, 23(1), 101–138. <https://doi.org/10.1007/s11831-014-9136-6>
- Kang, D. H., Yang, E., & Yun, T. S. (2019). Stokes-Brinkman flow simulation based on 3-D µ-CT images of porous rock using grayscale pore voxel permeability. *Water Resources Research*, 55(5), 4448–4464. <https://doi.org/10.1029/2018WR024179>
- Kaviany, M. (2012). *Principles of heat transfer in porous media*. Springer Science & Business Media.
- Kays, W. M., Crawford, M. E., & Weigand, B. (2005). *Convective heat and mass transfer*. McGraw-Hill.
- Keyes, D. E., McInnes, L. C., Woodward, C., Gropp, W., Myra, E., Pernice, M., et al. (2013). Multiphysics simulations: Challenges and opportunities. *The International Journal of High Performance Computing Applications*, 27(1), 4–83. <https://doi.org/10.1177/1094342012468181>
- Khatibi, M. (2017). Investigation on cuttings transportation in Non-Newtonian turbulent well flow advanced wellbore transport modeling (Ph.D. dissertation). University of Stavanger.
- Kirch, A., Razmara, N., Mamani, V. F. S., Meneghini, J. R., & Miranda, C. R. (2020). Multiscale molecular modeling applied to the upstream oil & gas industry challenges. *Polytechnica*, 3(1), 54–65. <https://doi.org/10.1007/s41050-019-00019-w>
- Kovscek, A. R. (2012). Emerging challenges and potential futures for thermally enhanced oil recovery. *Journal of Petroleum Science and Engineering*, 98(99), 130–143. <https://doi.org/10.1016/j.petrol.2012.08.004>
- Lesinigo, M., D'Angelo, C., & Quarteroni, A. (2011). A multiscale Darcy–Brinkman model for fluid flow in fractured porous media. *Numerische Mathematik*, 117(4), 717–752. <https://doi.org/10.1007/s00211-010-0343-2>
- Lewis, R. W. (1998). *The finite element method in the static and dynamic deformation and consolidation of porous media* (2nd ed.). John Wiley.
- Lv, Y., & Ekaterinaris, J. (2023). Recent progress on high-order discontinuous schemes for simulations of multiphase and multicomponent flows. *Progress in Aerospace Sciences*, 140, 100929. <https://doi.org/10.1016/j.paerosci.2023.100929>
- Maes, J., & Menke, H. P. (2022). GeoChemFoam: Direct modelling of flow and heat transfer in micro-CT images of porous media. *Heat and Mass Transfer*, 58(11), 1937–1947. <https://doi.org/10.1007/s00231-022-03221-2>
- Manning, C. E., & Aranovich, L. Y. (2014). Brines at high pressure and temperature: Thermodynamic, petrologic and geochemical effects. *Precambrian Research*, 253, 6–16. <https://doi.org/10.1016/j.precamres.2014.06.025>
- Mehmani, A., Prodanović, M., & Javadpour, F. (2013). Multiscale, multiphysics network modeling of shale matrix gas flows. *Transport in Porous Media*, 99(2), 377–390. <https://doi.org/10.1007/s11242-013-0191-5>
- Mohamed, M. M., Parimalarenganayaki, S., Khan, Q., & Murad, A. (2021). Review on the use of environmental isotopes for groundwater recharge and evaporation studies in the GCC countries. *Groundwater for Sustainable Development*, 12, 100546. <https://doi.org/10.1016/j.gsd.2021.100546>
- Mohan, A., & Tomar, G. (2024). Volume of fluid method: A brief review. *Journal of the Indian Institute of Science*, 104(1), 229–248. <https://doi.org/10.1007/s41745-024-00424-w>
- Mokheimer, E. M. A., Hamdy, M., Abubakar, Z., Shakeel, M. R., Habib, M. A., & Mahmoud, M. (2018). A comprehensive review of thermal enhanced oil recovery: Techniques evaluation. *Journal of Energy Resources Technology*, 141(3), 030801. <https://doi.org/10.1115/1.4041096>
- Mollaali, M., Kolditz, O., Hu, M., Park, C., Park, J., McDermott, C. I., et al. (2023). Comparative verification of hydro-mechanical fracture behavior: Task G of international research project DECOVALEX–2023. *International Journal of Rock Mechanics and Mining Sciences*, 170, 105530. <https://doi.org/10.1016/j.ijrmms.2023.105530>
- Murad, M. A., & Cushman, J. H. (2000). Thermomechanical theories for swelling porous media with microstructure. *International Journal of Engineering Science*, 38(5), 517–564. [https://doi.org/10.1016/S0020-7225\(99\)00054-3](https://doi.org/10.1016/S0020-7225(99)00054-3)
- Neale, G., & Nader, W. (1974). Practical significance of Brinkman's extension of Darcy's law: Coupled parallel flows within a channel and a bounding porous medium. *Canadian Journal of Chemical Engineering*, 52(4), 475–478. <https://doi.org/10.1002/cjce.5450520407>
- Nield, D. A. (2009). The Beavers–Joseph boundary condition and related matters: A historical and critical note. *Transport in Porous Media*, 78(3), 537–540. <https://doi.org/10.1007/s11242-009-9344-y>
- Nield, D. A., & Bejan, A. (2017). *Convection in porous media*. Springer International Publishing. <https://doi.org/10.1007/978-3-319-49562-0>
- Ochoa-Tapia, J. A., & Whitaker, S. (1995). Momentum transfer at the boundary between a porous medium and a homogeneous fluid—I. Theoretical development. *International Journal of Heat and Mass Transfer*, 38(14), 2635–2646. [https://doi.org/10.1016/0017-9310\(94\)00346-W](https://doi.org/10.1016/0017-9310(94)00346-W)
- Pal, B., & Ramaswamy, A. (2023). A multi-physics-based approach to predict mechanical behavior of concrete element in a multi-scale framework. *Mechanics of Materials*, 176, 104509. <https://doi.org/10.1016/j.mechmat.2022.104509>
- Peters, B., Baniasadi, M., Baniasadi, M., Besseron, X., Donoso, A. E., Mohseni, M., & Pozzetti, G. (2019). XDEM multi-physics and multi-scale simulation technology: Review of DEM–CFD coupling, methodology and engineering applications. *Particuology*, 44, 176–193. <https://doi.org/10.1016/j.partic.2018.04.005>

- Pham, T. A., Hashemi, A., Sutman, M., & Medero, G. M. (2023). Effect of temperature on the soil–water retention characteristics in unsaturated soils: Analytical and experimental approaches. *Soils and Foundations*, 63(3), 101301. <https://doi.org/10.1016/j.sandf.2023.101301>
- Pradeep, S., Arratia, P. E., & Jerolmack, D. J. (2024). Origins of complexity in the rheology of Soft Earth suspensions. *Nature Communications*, 15(1), 7432. <https://doi.org/10.1038/s41467-024-51357-y>
- Qiao, S., Ma, R., Wang, Y., Sun, Z., French, H. K., & Wang, Y. (2025). A new capillary and adsorption-force model predicting hydraulic conductivity of soil during freeze–thaw processes. *Water Resources Research*, 61(1), e2023WR036857. <https://doi.org/10.1029/2023WR036857>
- Quemada, D. (1977). Rheology of concentrated disperse systems and minimum energy dissipation principle. *Rheologica Acta*, 16(1), 82–94. <https://doi.org/10.1007/BF01516932>
- Radhakrishnan, R. (2021). A survey of multiscale modeling: Foundations, historical milestones, current status, and future prospects. *AIChE Journal*, 67(3), e17026. <https://doi.org/10.1002/aic.17026>
- Rathnaweera, T. D., Wu, W., Ji, Y., & Gamage, R. P. (2020). Understanding injection-induced seismicity in enhanced geothermal systems: From the coupled thermo-hydro-mechanical-chemical process to anthropogenic earthquake prediction. *Earth-Science Reviews*, 205, 103182. <https://doi.org/10.1016/j.earscirev.2020.103182>
- Rehman, M., Hafeez, M. B., & Krawczuk, M. (2024). A comprehensive review: Applications of the Kozeny–Carman model in engineering with permeability dynamics. *Archives of Computational Methods in Engineering*, 31(7), 3843–3855. <https://doi.org/10.1007/s11831-024-10094-7>
- Saasen, A., & Ytrehus, J. D. (2020). Viscosity models for drilling fluids—Herschel–Bulkley parameters and their use. *Energies*, 13(20), 5271. <https://doi.org/10.3390/en13205271>
- Schott, J., Pokrovsky, O. S., & Oelkers, E. H. (2009). The link between mineral dissolution/precipitation kinetics and solution chemistry. *Reviews in Mineralogy and Geochemistry*, 70(1), 207–258. <https://doi.org/10.2138/rmg.2009.70.6>
- Singh, K. (2019). How hydraulic properties of organic matter control effective liquid permeability of Mudrocks. *Transport in Porous Media*, 129(3), 761–777. <https://doi.org/10.1007/s11242-019-01305-y>
- Soulaine, C., Creux, P., & Tchelepi, H. (2019). Micro-continuum framework for pore-scale multiphase fluid transport in shale formations. *Transport in Porous Media*, 127(1), 85–112. <https://doi.org/10.1007/s11242-018-1181-4>
- Soulaine, C., Gjetvaj, F., Garing, C., Roman, S., Russian, A., Gouze, P., & Tchelepi, H. A. (2016). The impact of sub-resolution porosity of X-ray microtomography images on the permeability. *Transport in Porous Media*, 113(1), 227–243. <https://doi.org/10.1007/s11242-016-0690-2>
- Souley, M., Vu, M.-N., Coarita-Tintaya, E. D., Armand, G., & Golfier, F. (2024). Effect of short- and long-term nonlinear behaviour on the thermoporo-mechanical pressurisation in CO₂ claystone. *International Journal of Rock Mechanics and Mining Sciences*, 175, 105650. <https://doi.org/10.1016/j.ijrmms.2024.105650>
- Spearman, J. (2017). An examination of the rheology of flocculated clay suspensions. *Ocean Dynamics*, 67(3–4), 485–497. <https://doi.org/10.1007/s10236-017-1041-8>
- Sun, W. C., Andrade, J. E., & Rudnicki, J. W. (2011). Multiscale method for characterization of porous microstructures and their impact on macroscopic effective permeability. *International Journal for Numerical Methods in Engineering*, 88(12), 1260–1279. <https://doi.org/10.1002/nme.3220>
- Tan, P., Jin, Y., Han, K., Zheng, X., Hou, B., Gao, J., et al. (2017). Vertical propagation behavior of hydraulic fractures in coal measure strata based on true triaxial experiment. *Journal of Petroleum Science and Engineering*, 158, 398–407. <https://doi.org/10.1016/j.petrol.2017.08.076>
- Tryggvason, G., Dabiri, S., Aboulhasanzadeh, B., & Lu, J. (2013). Multiscale considerations in direct numerical simulations of multiphase flows. *Physics of Fluids*, 25(3), 031302. <https://doi.org/10.1063/1.4793543>
- van Genuchten, M. T. (1980). A closed-form equation for predicting the hydraulic conductivity of unsaturated soils. *Soil Science Society of America Journal*, 44(5), 892–898. <https://doi.org/10.2136/sssaj1980.03615995004400050002x>
- Vargaftik, N. B., Volkov, B. N., & Voljak, L. D. (1983). International tables of the surface tension of water. *Journal of Physical and Chemical Reference Data*, 12(3), 817–820. <https://doi.org/10.1063/1.555688>
- Vilarrasa, V., & Rutqvist, J. (2017). Thermal effects on geologic carbon storage. *Earth-Science Reviews*, 165, 245–256. <https://doi.org/10.1016/j.earscirev.2016.12.011>
- Wagner, W., & Prüß, A. (2002). The IAPWS formulation 1995 for the thermodynamic properties of ordinary water substance for general and scientific use. *Journal of Physical and Chemical Reference Data*, 31(2), 387–535. <https://doi.org/10.1063/1.1461829>
- Wang, D. (2019). *Direct numerical simulation of coupled fluid-particle flow in hydraulic fractures*. (PhD Thesis). The University of Queensland. <https://doi.org/10.14264/uql.2019.629>
- Wang, Q., Guo, S., Ali, M., Song, X., Tang, Z., Zhang, Z., et al. (2022). Thermally enhanced bioremediation: A review of the fundamentals and applications in soil and groundwater remediation. *Journal of Hazardous Materials*, 433, 128749. <https://doi.org/10.1016/j.jhazmat.2022.128749>
- Wang, Y., Chung, E., Fu, S., & Huang, Z. (2021). A comparison of mixed multiscale finite element methods for multiphase transport in highly heterogeneous media. *Water Resources Research*, 57(5), e2020WR028877. <https://doi.org/10.1029/2020WR028877>
- Wang, Y., de Hoop, S., Voskov, D., Bruhn, D., & Bertotti, G. (2021). Modeling of multiphase mass and heat transfer in fractured high-enthalpy geothermal systems with advanced discrete fracture methodology. *Advances in Water Resources*, 154, 103985. <https://doi.org/10.1016/j.advwatres.2021.103985>
- Wang, Y., Shi, L., Hu, X., Song, W., & Wang, L. (2023). Multiphysics-informed neural networks for coupled soil hydrothermal modeling. *Water Resources Research*, 59(1), e2022WR031960. <https://doi.org/10.1029/2022WR031960>
- Weishaupt, K., Joekar-Niasar, V., & Helmig, R. (2019). An efficient coupling of free flow and porous media flow using the pore-network modeling approach. *Journal of Computational Physics*, 381, 100011. <https://doi.org/10.1016/j.jcp.2019.100011>
- Wendt, J. F. (Ed.). (2008). *Computational fluid dynamics: An introduction* (3rd ed.). Springer.
- Whitaker, S. (1999). Volume averaging of transport equations. In *The method of volume averaging* (pp. 1–60). Kluwer Academic Publishers.
- Wibberley, C. A. J., & Shimamoto, T. (2005). Earthquake slip weakening and asperities explained by thermal pressurization. *Nature*, 436(7051), 689–692. <https://doi.org/10.1038/nature03901>
- Wong, C. P., Jiang, B., Bohn, T. J., Lee, K. N., Lettenmaier, D. P., Ma, D., & Ouyang, Z. (2017). Lake and wetland ecosystem services measuring water storage and local climate regulation. *Water Resources Research*, 53(4), 3197–3223. <https://doi.org/10.1002/2016WR019445>
- Wu, L., Gomez-Velez, J. D., Krause, S., Singh, T., Wörman, A., & Lewandowski, J. (2020). Impact of flow alteration and temperature variability on hyporheic exchange. *Water Resources Research*, 56(3), e2019WR026225. <https://doi.org/10.1029/2019WR026225>
- Yin, S., Towler, B. F., Dusseault, M. B., & Rothenburg, L. (2010). Fully coupled THMC modeling of wellbore stability with thermal and solute convection considered. *Transport in Porous Media*, 84(3), 773–798. <https://doi.org/10.1007/s11242-010-9540-9>
- Yu, Z., Shao, J.-F., Vu, M.-N., & Armand, G. (2021). Numerical study of thermo-hydro-mechanical responses of in situ heating test with phase-field model. *International Journal of Rock Mechanics and Mining Sciences*, 138, 104542. <https://doi.org/10.1016/j.ijrmms.2020.104542>

- Zagorščak, R., Sedighi, M., & Thomas, H. R. (2017). Effects of thermo-osmosis on hydraulic behavior of saturated clays. *International Journal of Geomechanics*, 17(3), 04016068. [https://doi.org/10.1061/\(ASCE\)GM.1943-5622.0000742](https://doi.org/10.1061/(ASCE)GM.1943-5622.0000742)
- Zhang, X., Zhang, Y., Qi, J., Marek, G. W., Srinivasan, R., Feng, P., et al. (2025). Effects of changes in freeze-thaw cycles on soil hydrothermal dynamics and erosion degradation under global warming in the black soil region. *Water Resources Research*, 61(3), e2024WR038318. <https://doi.org/10.1029/2024WR038318>
- Zhao, J., & Brown, E. T. (1992). Thermal cracking induced by water flow through joints in heated granite. *International Journal of Rock Mechanics and Mining Sciences & Geomechanics Abstracts*, 29(1), 77–82. [https://doi.org/10.1016/0148-9062\(92\)91047-9](https://doi.org/10.1016/0148-9062(92)91047-9)
- Zheng, X., & Bourg, I. C. (2023). Nanoscale prediction of the thermal, mechanical, and transport properties of hydrated clay on 106- and 1015-fold larger length and time scales. *ACS Nano*, 17(19), 19211–19223. <https://doi.org/10.1021/acsnano.3c05751>
- Zheng, X., & Espinoza, D. N. (2021a). Measurement of unloading pore volume compressibility of Frio sand under uniaxial strain stress path and implications on reservoir pressure management. *Rock Mechanics and Rock Engineering*, 54(11), 5745–5760. <https://doi.org/10.1007/s00603-021-02571-3>
- Zheng, X., & Espinoza, D. N. (2021b). Multiphase CO₂-brine transport properties of synthetic fault gouge. *Marine and Petroleum Geology*, 129, 105054. <https://doi.org/10.1016/j.marpetgeo.2021.105054>
- Zheng, X., Underwood, T. R., & Bourg, I. C. (2023). Molecular dynamics simulation of thermal, hydraulic, and mechanical properties of bentonite clay at 298 to 373 K. *Applied Clay Science*, 240, 106964. <https://doi.org/10.1016/j.clay.2023.106964>